RSC Advances

PAPER

View Article Online
View Journal | View Issue

Cite this: *RSC Adv.*, 2025, **15**, 20552

Hybrid thiazolyl–benzylidene–phenol metal complexes as novel chemotherapeutic agents with anti-topoisomerase I activity in human breast carcinoma: synthesis, *in vitro* and *in silico* studies†

Ahmed M. Alharbi,[a] Mona Katary,[bc] Khulud M. Alshehri,[d] Basim H. Asghar,[e] Mohmed M. Omran,[f] Reda F. M. Elshaarawy,[gh] Amira Mili,[i] Hani S. Hafez*[j] and Rozan Zakrya[k]

Received 6th February 2025
Accepted 6th June 2025

DOI: 10.1039/d5ra00889a

rsc.li/rsc-advances

A new ligand, benzylidene–phenol–thiazole (HBHTP), and its M(II) complexes (M = Co, Ni, Cu, or Zn) were synthesized using a hybrid pharmacophore approach. The structures were optimized using density functional theory (DFT) calculations. MTT cytotoxicity assay showed that CuBHTP was the most effective and least toxic to normal cells, with the highest toxicity against MCF-7 cells. CuBHTP was more selective than staurosporine, with a selectivity index (SI) of 4.2 for cancer MCF-7 cells compared to 2.5 for healthy MCF10a cells. Compared with novobiocin, it exhibited significant inhibitory effects on aromatase cytochrome 19A and reduced Hsp90 expression. The treatment also revealed significant upregulation of the apoptotic marker P53 and inhibitory effects on tubulin β, SULF1,2, and bFGF gene expression levels compared to the untreated MCF7 carcinoma. Furthermore, CuBHTP significantly inhibited topoisomerase I and cell proliferation by inducing cell cycle arrest in G1 and S phases. The CuBHTP complex is a highly effective anticancer agent, and molecular docking studies have confirmed its binding to grooves and topoisomerase I. Therefore, ligand/copper may shed new light on the inhibitory mechanisms of cancer cell proliferation through its ability to form DNA adducts.

1 Introduction

The incidence of breast cancer (BC), the most common cancer among women, has markedly increased over the past decade.[1] The heterogeneity of BC, with up to ten molecular subtypes, challenges the development of effective treatments. Conventional chemotherapy remains the primary treatment for patients with BC, but there are limited molecular therapeutic options. Clinical management is challenging because of the restricted therapies and clinicopathological heterogeneity. Apoptosis is critical for growth and homeostasis of multicellular organisms. Surviving cells with DNA damage contribute to cancer progression. Cancer cells exhibit morphological features such as membrane blebbing, chromatin condensation, and apoptotic bodies.[2]

Topoisomerase I (TOPI), a type IB enzyme, controls the DNA structure during transcription, recombination, replication, and repair.[3] It breaks one strand, causing single-strand breaks in DNA. Cancer cells require a high TOPI activity for rapid division, and their inhibition can cause double-strand breaks and cell death. Topoisomerase I inhibitors, including camptothecin, exhibit dose-limiting adverse effects and poor water solubility, which lead to bone marrow toxicity and gastrointestinal disorders. Developing novel topoisomerase I inhibitors with reduced

---

[a] Department of Chemistry, Faculty of Sciences, Umm Al-Qura University, Makkah, Saudi Arabia. E-mail: amaharbi@uqu.edu.sa

[b] Chemistry Department, Faculty of Science, Port-Said University, Port-Said, Egypt. E-mail: monakatary@gmail.com

[c] Department of Basic Sciences, Horus University, Egypt. E-mail: mkatary@horus.edu.eg

[d] Department of Biology, Al-Baha University, Saudi Arabia. E-mail: kalshehri@bu.edu.sa

[e] Department of Chemistry, Faculty of Sciences, Umm Al-Qura University, Makkah, Saudi Arabia. E-mail: bhasghar@uqu.edu.sa

[f] Chemistry Department, Faculty of Science, Helwan University, Helwan, Egypt. E-mail: Mohmed.Omran@gmail.com

[g] Department of Chemistry, Faculty of Science, Suez University, 43533 Suez, Egypt. E-mail: reda.elshaarawy@suezuniv.edu.eg

[h] Institut für Anorganische Chemie und Strukturchemie, Heinrich-Heine Universität Düsseldorf, Düsseldorf, Germany

[i] Department of Biology, Al-Baha University, Al Aqiq, Saudi Arabia. E-mail: ahajsalah@bu.edu.sa

[j] Department of Zoology, Faculty of Science, Suez University, 43533 Suez, Egypt. E-mail: hani.hafez@suezuniv.edu.eg

[k] Chemistry Department, Faculty of Science, Port-Said University, Port-Said, Egypt. E-mail: rzakrya@yahoo.com

† Electronic supplementary information (ESI) available: Experimental section (materials, spectral data, and computational analysis), tables (Tables S1–S6), and figures (Fig. S1–S4). See DOI: **https://doi.org/10.1039/d5ra00889a**

side effects is crucial, as these agents effectively impair cancer cell genetic stability[4] and induce DNA strand breaks.[5,6] TOPI–DNA cleavage complexes (TOPIcc) are formed by inhibition of re-ligation by carnitine palmitoyltransferase (CPT) in the TOPI catalytic cycle. TOPIcc exhibits cytotoxic activity during the S-phase because its interaction with the replication machinery leads to DNA breakdown and cell death.[7]

Molecular hybridization is a promising strategy for drug design, particularly for anticancer therapy. By combining multiple pharmacophores into a single entity, hybrid drug design offers the potential to overcome limitations associated with conventional anticancer drugs. The ability to address pharmacokinetic limitations and enhance therapeutic efficacy is crucial for the development of innovative treatments.[8] As advancements in this field continue, molecular hybridization holds great promise in the development of novel and effective anticancer therapies.

Thiazoles are important in medicinal chemistry because of their wide range of biological activities, which make them valuable for drug discovery. Synthesis of thiazole-based therapeutic agents is central to the development of effective treatments for various diseases. These compounds can significantly affect drug discovery and therapeutic development. Tiazofurin, dasatinib,[9] and thiazole hybrids have shown promising results in clinical trials for cancer therapy.[10] Benzylidene derivatives have gained attention in pharmaceutical research because of their diverse biological activities, demonstrating potential in anticancer,[11] antimicrobial, antiviral,[12,13] anti-inflammatory, and antioxidant applications. Phenol derivatives are promising candidates owing to their antimicrobial, antioxidant, and anti-inflammatory properties.[14] Combretastatin A4, which combines benzylidene and phenol pharmacophores, has emerged as a promising anticancer agent that targets the tumor vasculature, making it valuable for clinical applications.[15]

When designing novel metal-based anticancer agents, the selection of appropriate metal ions is crucial, because their properties significantly affect the stability, reactivity, and pharmacological activity of the resulting complexes. We selected cobalt (Co), nickel (Ni), copper (Cu), and zinc (Zn) for complexation with the novel ligand benzylidene–phenol–thiazole (HBHTP), based on their coordination chemistry, redox behavior, and biological significance. Cobalt(II) was selected for its ability to form stable octahedral complexes and redox activity, which can induce oxidative stress in cancer cells.[16] Cobalt complexes have shown promise for interacting with DNA and inhibiting topoisomerase.[17] Nickel(II) was chosen because of its capacity to form square-planar or octahedral complexes that facilitate DNA intercalation, potentially disrupting cancer cell proliferation. Nickel complexes have been shown to be cytotoxic to cancer cell lines.[18] Copper(II) was prioritized because of its biological relevance and redox properties, which enable the generation of reactive oxygen species (ROS) that target cancer cells.[19] Copper complexes exhibit anticancer potential through DNA-binding, topoisomerase inhibition, and modulation of signalling pathways.[19] Zinc(II) was selected because of its role as an enzyme cofactor and its ability to form tetrahedral complexes. Zinc complexes have the potential to stabilize DNA-binding motifs and inhibit tumor-associated enzymes.[20] These metals were chosen for their ability to form complexes with nitrogen- and oxygen-containing ligands such as HBHTP.[21] By studying these metal complexes, we aimed to understand how metal ion properties influence their anticancer activity and mechanisms of action, following the hybrid pharmacophore strategy to enhance their therapeutic efficacy.

The present study was constructed into two pathways with the following two aims: (1) to use molecular hybridization to construct a new thiazole hybrid (HBHTP) (Fig. 1) and its metal(II) complexes (M = Co, Ni, Cu, Zn) to investigate their biological role in minimizing and diminishing cellular proliferation and induction of apoptotic mechanisms through cell cycle arrest, DNA content, P53 expression, and triggering apoptosis; and (2) to investigate the role of the synthesized thiazole hybrid and its metal complexes in inhibiting the gene expression of aromatase, sulfatase (Sulf1,2), and basic fibroblast growth factor (bFGF), which are the main factors that affect tumorigenesis, recurrence, and treatment resistance, and

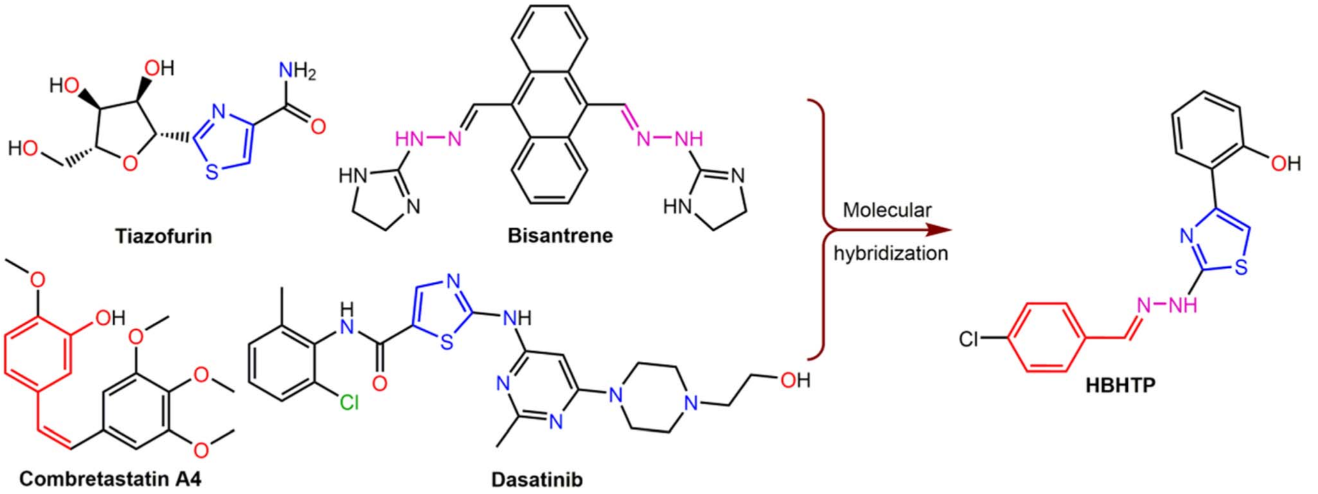

Fig. 1 Design of thiazole hybrid by combining multiple pharmacophores.

their ability to inhibit topoisomerase and form CT adducts through the metals.

2 Materials and methods

The ESI† contains the specifications of the reagents and their commercial suppliers. Analytical grade organic solvents were supplied by ADWIC Chemical Reagent Co. Ltd (Cairo, Egypt). 2-(4-Chlorobenzylidene)hydrazine-1-carbothioamide (**1**) was obtained from a previous study. The experimental method used to prepare 2-hydroxyphenacyl bromide (**2**) is described in the ESI.† Silica gel plates were used for thin-layer chromatography (TLC) to monitor reactions. The ESI† provides a complete description of the devices used for the characterization of novel compounds.

2.1. Synthesis of 2-(2-(2-(4-chlorobenzylidene)hydrazineyl)thiazol-4-yl)phenol (HBHTP, 3)

The ligand was prepared following a protocol adapted from Saydam and Yilmaz,[22] however, with slight modifications. Briefly, thiosemicarbazone (**1**) (0.42 g, 2 mmol, 2.0 equiv.) anhydrous sodium acetate (0.66 g, 8 mmol, 8.0 equiv.) and ethanol (40 mL) were added to a 100 mL round-bottom flask (RBF). After stirring the content for 10 min at room temperature, 2-hydroxyphenacyl bromide (**2**) (0.43 g, 2 mmol, 2.0 equivalent) was added, and the reaction mixture was allowed to reflux for 6–8 h. The progress and completion of the reaction were monitored by TLC, using a mixture of chloroform/ethyl acetate (9 : 1) as the mobile phase. After cooling to ambient temperature, the precipitate was collected by filtration, washed with ethanol (3 × 5 mL), and dried under vacuum to yield HBHTP. The product was obtained as a faint yellow solid in an 81% yield. mp 221–223 °C. The details of the structural characterization of the ligand are provided in the ESI.†

2.2. General procedure for the preparation of metal complexes (4a–d)

The ligand was prepared following a protocol adapted from Saydam and Yilmaz,[22] however, with slight modifications. Briefly, an ethanolic solution of the ligand (1.0 mmole HBHTP/10 mL EtOH) and metal(II) chlorides (1.0 mmole salt/10 mL EtOH) was refluxed for 5 h in the presence of three drops of an aqueous ammonia solution to produce the corresponding M(II) complexes (M = Co, Ni, Cu, Zn). After the allotted reflux time, the reaction mixture was allowed to cool to room temperature and the solid products were filtered out. The products were collected, washed three times with 3 mL ethanol, and dried overnight under vacuum at room temperature.

2.2.1 $[Co(BHTP)_2]\cdot H_2O$ ($Co(BHTP)_2$, 4a). Pink solid (62%). FTIR (KBr, cm^{-1}): 3552 (s, sh), 3449 (s, br), 3162 (s, br), 1597 (s, sh), 1567 (s, sh), 1487 (s, sh), 1453 (m, sh), 1402 (m, sh), 1318 (m, sh), 1280 (m, sh), 1115 (m, sh), 1090 (m, sh), 1012 (m, sh), 924 (m, sh), 821 (s, sh), 751 (m, sh), 699 (m, sh), 584 (m, sh), 490 (m, sh). MALDI-TOF (dithranol (DIT)) *m*/*z*: 227.0 $[DIT]^+$, 330.5 $[LH]^+$, 734.5 $[M]^+$, 960.5 $[M(DIT)]^+$ (M = complex). Anal. calcd for $C_{32}H_{24}Cl_2CoN_6O_3S_2$ (734.54 g mol^{-1}): C, 52.33; H, 3.29; N, 11.44; S, 8.73%. Found: C, 52.29; H, 3.38; N, 11.26; S, 8.65%.

2.2.2 $[Ni(BHTP)_2]\cdot H_2O$ ($Ni(BHTP)_2$, 4b). Pale green solid (59%). FTIR (KBr, cm^{-1}): 3445 (s, br), 3278 (s, br), 3164 (s, br), 1606 (s, sh), 1503 (s, sh), 1446 (m, sh), 1405 (m, sh), 1321 (m, sh), 1282 (w, sh), 1120 (m, sh), 1092 (m, sh), 1014 (m, sh), 861 (m, sh), 820 (s, sh), 754 (m, sh), 669 (m, sh), 515 (m, sh), 491 (m, sh). MALDI-TOF (dithranol (DIT)), *m*/*z*: 227.0 $[DIT]^+$, 330.4 $[LH]^+$, 716.3 $[Ni(BHTP)_2]^+$, 960.5 $[Ni(BHTP)_2(DIT)]^+$. Anal. calcd for $C_{32}H_{24}Cl_2N_6NiO_3S_2$ (734.30 g mol^{-1}): C, 52.34; H, 3.29; N, 11.45; S, 8.73%. Found: C, 52.21; H, 3.33; N, 11.37; S, 8.70%.

2.2.3 $[Cu(BHTP)_2]\cdot 2H_2O$ (CuBHTP, 4c). Green-blue solid (67%). FTIR (KBr, cm^{-1}): 3435 (s, br), 3333 (s, br), 3161 (s, sh), 1598 (s, sh), 1550 (s, sh), 1488 (m, sh), 1406 (m, sh), 1315 (m, sh), 1277 (m, sh), 1089 (m, sh), 1012 (m, sh), 959 (m, sh), 823 (s, sh), 754 (m, sh), 618 (m, sh), 513 (m, sh), 441 (m, sh). MALDI-TOF (dithranol (DIT)) *m*/*z*: 227.0 $[DIT]^+$, 330.4 $[LH]^+$, 721.3 $[Cu(BHTP)_2]^+$, 947.4 $[Cu(BHTP)_2(DIT)]^+$. Anal. calcd for $C_{32}H_{26}Cl_2CuN_6O_4S_2$ (757.16 g mol^{-1}): C, 50.76; H, 3.46; N, 11.10; S, 8.47%. Found: C, 50.69; H, 3.54; N, 11.08; S, 8.42%.

2.2.4 $[Zn(BHTP)_2]\cdot H_2O$ (ZnBHTP, 4d). Dirty white (58%). FTIR (KBr, cm^{-1}): 3568 (s, sh), 3439 (s, br), 3169 (s, br), 1599 (s, sh), 1489 (s, sh), 1455 (m, sh), 1404 (s, sh), 1279 (m, sh), 1090 (m, sh), 1012 (m, sh), 925 (m, sh), 872 (m, sh), 819 (s, sh), 750 (m, sh), 696 (m, sh), 585 (m, sh), 513 (w, sh), 441 (w, sh). MALDI-TOF (dithranol (DIT)), *m*/*z*: 227.0 $[DIT]^+$, 330.3 $[LH]^+$, 770.5 $[M]^+$, 966.7 $[M(DIT)]^+$ (M = complex). Anal. calcd for $C_{32}H_{24}Cl_2N_6O_3S_2Zn$ (740.68 g mol^{-1}): C, 51.87; H, 3.26; N, 11.34; S, 8.65%. Found: C, 51.73; H, 3.33; N, 11.23; S, 8.59%.

2.3. *In silico* studies

Molecular docking studies were conducted following geometry optimization of the benzylidene–phenyl–thiazole (HBHTP) ligand and its copper complex (CuBHTP). The optimized compounds were subjected to an active-site molecular docking simulation after converting their file formats into PDBQT using the Open Babel software (version 2.3.2). The protein molecular target (topoisomerase I ID: 1T8I) was downloaded from the Protein Data Bank PDB (https://www.rcsb.org). The targeted protein was prepared by removing all heteroatoms and water molecules using the Biovia Discovery Studio software. SWISS-PDBVIEWER (version 4.1.0) (SPDBV) was used to minimize energy consumption and check for any missing parts of the selected receptor. AutoDock 4.2 software[23] was used to implement the active-site molecular docking process. The process began with the incorporation of polar hydrogens into the targeted protein, followed by the inclusion of Kollman charges and the assignment of Gasteiger charges. The grid box was configured to cover the entire active site of the protein, spanning (60, 60, 60) points along the attributes ($X = 23.255$, $Y = -5.866$, $Z = 30.659$) with a spacing of 0.375. The docking parameters were managed using genetic algorithms, 50 conformations/poses were detected, and the best conformer was selected considering the lowest free energy of binding, which is represented by ligand-receptor non-covalent interactions (NCIs). LigPlus (LigPlot+ v.2.2.8) was used to study the hydrophobic interactions between docked drug-like molecules and the target protein. The best pose and the 3D and 2D images of the best conformers were visualized using Biovia Discovery Studio.

2.4. Cytotoxicity and cell viability assay

The human breast cancer cell line MCF-7 and human breast epithelial cell line MCF10A were obtained from the VACSERA Tissue Culture Unit in Egypt. The MTT test was used to evaluate the *in vitro* cytotoxicity of the newly synthesized HBHTP ligand (**3**) and its complexes (**4a–d**) against human breast carcinoma (MCF-7) to induce endothelial cell death, in comparison with the clinical anticancer medication staurosporine (STP) as a positive control. MCF-7 and MCF10A cells were seeded in triplicate in 96-well Corning plates and treated with 50 μM of each compound. The MTT reagent was added 72 h post-treatment, followed by a 4 hour incubation period.[24] The formazan crystals were then dissolved in 100 μL of dimethyl sulfoxide (DMSO), and the absorbance was measured at 570 nm and 630 nm using a ROBONIK P2000 ELIZA multi-detection microplate reader. The effects of chemicals on cell viability were determined using the following equation:

$$\text{Relative cell viability }(\%) = \frac{A - A_0}{A_{\text{NC}} - A_0}$$

A: absorbance of the tested compound; A_0: absorbance of the blank (no cells, positive control); A_{NC}: absorbance of the negative control (only cells, no treatment).

2.5. Aromatase (CYP19A) activity assay kit (fluorometric)

The CuBHTP was tested using an *in vitro* aromatase inhibition assay. Aromatase inhibition was quantified by measuring the fluorescence intensity of fluorescein standards using an aromatase (CYP 19A) Activity Assay Kit (Biovision).[25] Briefly, CuBHTP was preincubated with a reaction mixture containing the enzyme and substrate for 60 min at 37 °C. Subsequently, the fluorescence of the mixture was measured using a TECAN fluorescence spectrophotometer (1038708 Männedorf, Switzerland) at excitation and emission wavelengths of 488 nm and 527 nm, respectively.

2.6. Enzyme-linked immunosorbent assay quantitative estimation of Hsp90 and P53

The effect of CuBHTP on HSP90α expression in MCF-7 cells was compared with that of the control group treated with novobiocin, a potent inhibitor of HSP90α that triggers DNA-triggered apoptosis in MCF-7 breast cancer cells, using a screening assay kit (BPS Bioscience catalog # 50317) and cell homogenates specifically designed for HSP90α (C-terminal) inhibition.

Tumor suppressor protein P53 was assessed using an assay kit (NB 200-103). Homogenized cells were stored at −80 °C and centrifuged. The optical density was measured using a microplate reader at 450 nm. Average absorbance values were calculated for the standards, controls, and samples. A standard curve was plotted using the mean absorbance against concentration. The data were normalized to β-actin levels and expressed in ng mL^{-1} using a calibration curve from the Hsp90 dilutions. This was repeated twice using a ROBONIK P2000 ELISA READER (MIDC Industrial Area, Mahape, Navi Mumbai – 400710, India).

2.7. Tubulin β enzyme assay

In vitro assessment of β-tubulin in the tissue homogenate extracts was performed using a Simple-Step ELISA kit.[26] The cells were grown in DMEM (Invitrogen/Life Technologies) supplemented with 10% FBS (Hyclone), 10 mg per mL insulin (Sigma), and 1% penicillin–streptomycin. The cells were plated at a density of 1.2–1.8 × 10 000 cells per well in 100 μL of complete growth medium supplemented with 100 μL of the compound per well in a 96-well plate and incubated for 24 h. Tubulin was estimated using Tecan-spark READER (1038708 Männedorf, Switzerland) at an excitation wavelength of 360 nm and an emission wavelength of 450 nm.

2.8. Annexin V-FITC apoptosis detection

MCF-7 cells were seeded at a density of 1.0 × 105 cells per well in 6-well microtiter plates. After 24 h, the HCPT and lycorine solutions were used at concentrations of 3, 6, and 12 μmol L^{-1}. An equal volume of RPMI-1640 medium was added to the control group. The cells were cultured for 48 h at 37 °C in a CO_2 incubator. The supernatant was discarded and the cells were resuspended in a solution containing 100 000 cells and phosphate-buffered saline (PBS). The cells were then mixed with propidium iodide (PI) and Annexin V-FITC and analyzed by flow cytometry (BD Biosciences, 2350 Qume Drive, San Jose, California 95131, United States) in an ice bath. The cell suspension was filtered through a 300-mesh nylon mesh before detection at an excitation wavelength of 488 nm and an emission wavelength of 525 nm.[27]

2.9. Propidium iodide flow cytometry kit for cell cycle analysis

The cell cycle phases of MCF-7 cells were examined using a propidium iodide (PI) flow cytometry kit (ab139418).[28] The cells were washed with phosphate-buffered saline, fixed with 70% ethanol for 30 min, centrifuged, washed twice with PBS, and stained with propidium iodide (PI). Cells were treated with ribonuclease A and 400 μL PI solution per million cells and incubated for 5–10 minutes at room temperature. The labeled cells were assessed by flow cytometry in a solution containing PI and RNase A using a BD FACS Caliber instrument (2350 Qume Drive, San Jose, California 95131, United States).

2.10. Quantitative real-time (qPCR) estimation

Reverse transcriptase (RT) was used to produce complementary DNA (cDNA) by quantitative real-time PCR. Total mRNA was extracted from MCF-7 cells using the SV Total RNA Isolation System. SYBR Green I was used for real-time PCR (Applied Biosystems Real-Time PCR Instruments) amplification using Applied Biosystems software version 3.1. ATG gene expression, internal control (GAPDH gene expression), and non-template control (water) cDNA samples were amplified in duplicate by qPCR. The master mix in the PCR tubes was thoroughly mixed, without bubbling.[29]

The sulfatase 1 SULF1: F5′-AGACAGCCACTCACCTCTTCAG-3, R-5′TTCTGCCAGTGCCTCTTTGCTG-3′; SULF2: F5′-CTAGCTAG-CAAAAAAGAAGATGGGCCCCC-3′, R-5′-CGGGATCCTTAACCTTCC-CAGCCTTCCC-3′; bFGF: 5′-TCTTCCTGCGCATCCACC-3′ and reverse 5′-TCAGCTCTTAGCAGACATTGGAAGA-3′; TOPI 5′-GAA-CAAGCAGCCCGAGGATGAT-3′ and 5′-TGCTGTAGCGTGATG-GAGGCAT-3′; TOPII: 5′-GGTCAGTTTGGAACTCGGCTTC-3′ and 5′-AGGAGGTTGTCATCCACAGCAG-3′ and housekeeping genes (GAPDH) were analyzed, and the Ct values were noted on the PCR data sheet for each of these genes. A correlation between the expression of the internal control and target genes was observed, as was the evaluation of gene expression in the control sample.

2.11. Statistical analyses

Measurements were performed in quadruplicate for each experiment. One-way and two-way ANOVA were used with a significance threshold of $P < 0.05$, to determine the significance of the differences between the experimental groups. Data are presented as mean ± standard deviation (SD). IC_{50} values were determined using GraphPad Prism (v9.0) and standard errors (SE) were obtained from repeated measurements. Furthermore, 95% confidence intervals (CI) were calculated to evaluate the accuracy of IC_{50} estimates.

3 Results and discussion

3.1. Chemistry

A step-by-step protocol used to prepare the thiazolylphenol ligand (HBHTP, **3**) and its metal complexes is shown in Scheme 1. 4-Chlorobenzaldehyde was initially employed as a precursor to generate 4-chlorobenzylidene thiosemicarbazone (**2**) *via* a Schiff base condensation reaction with thiosemicarbazide in ethanol under reflux. α-Bromination of 2-hydroxyacetophenone was performed by reacting it with a mixture of Br_2 and CH_3COOH under stirring at room temperature to obtain phenacyl bromide (**2**). The desired ligand (HBHTP, **3**) was obtained *via* intermolecular cyclocondensation by refluxing the ethanolic mixture of thiosemicarbazone (**1**) and phenacyl bromide (**2**) in the presence of a catalytic amount of anhydrous AcONa. To prepare metal(II) BHTP complexes, HBHTP was refluxed with $M(II)Cl_2\cdot xH_2O$ in an ethanolic solution with the addition of ammonia as a deprotonating agent (Scheme 1).

3.2. Structural characterization

A new thiazolylphenol ligand (HBHTP, **3**) and its M(II) complexes were obtained in reasonable yield. Consequently, the structures of the complexes were determined through elemental and spectral analyses, including FTIR, UV-vis, and magnetic measurements. The structures were compared with those of previously reported metal complex analogs (Table S1, ESI†). The elemental analysis results (CHNS) not only verified that the new compounds were formed successfully but also supported their proposed molecular structures.

3.2.1. MALDI-TOF mass spectrometry. MALDI-TOF mass spectral analysis of the synthesized metal complexes was performed using dithranol (DIT, 226.23 g mol^{-1}) as the MALDI matrix to confirm their composition and structural integrity. Fig. S1–S4 (ESI†) show MALDI spectra of the metal complexes of the HBHTP ligand (L). These figures, along with the experimental section, reveal the presence of peaks corresponding to $[DIT]^+$ $[LH]^+$, $[ML_2]^+$, and $[ML_2(DIT)]^+$ for all the complexes. The detection of the $[ML_2]^+$ and $[ML_2(DIT)]^+$ species suggests that the metal complexes are stable and can be observed in their

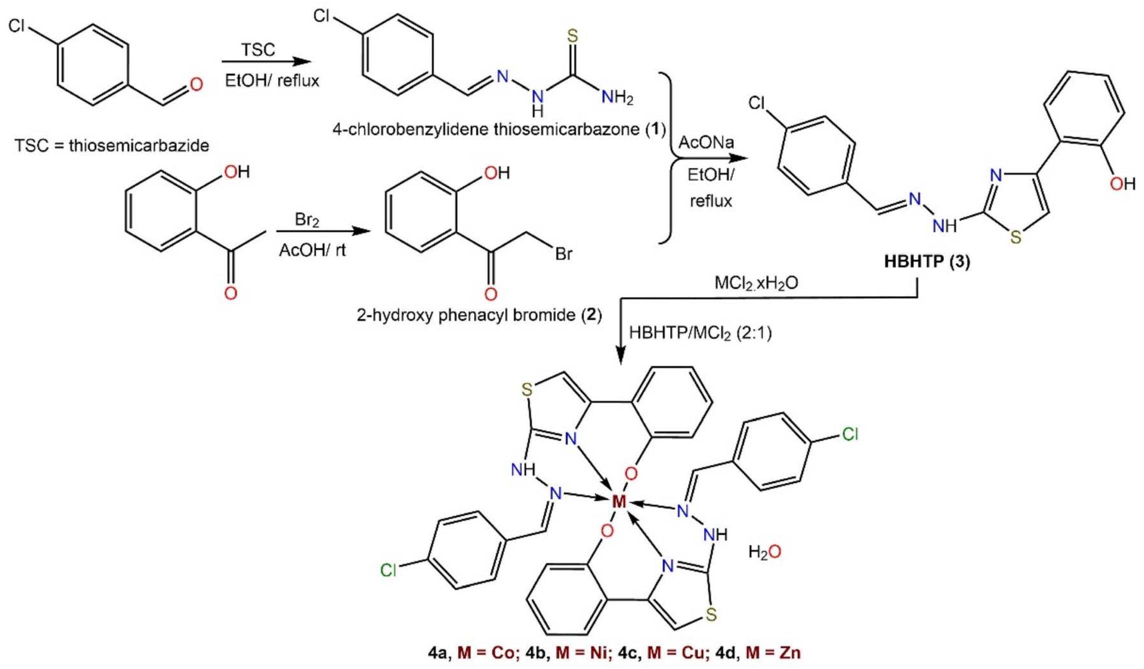

4a, M = Co; **4b**, M = Ni; **4c**, M = Cu; **4d**, M = Zn

Scheme 1 The step-by-step protocol used for the preparation of thiazolyl–phenol ligand (HBHTP, **3**) and its complexes.

intact forms, whereas the peaks for [DIT]$^+$ and [LH]$^+$ may result from the fragmentation or ionization of the MALDI matrix and ligands.

3.2.2. Fourier transform infrared spectroscopy (FTIR). Fig. 2A shows the FTIR spectra of the thiazole hybrid ligand (HBHTP, **3**) in its free form and in complex with M(II) ions. The phenolic OH and hydrazineyl NH groups in the HBHTP ligand are responsible for the presence of a broad band in the range of 3228–3465 cm^{-1} and another band at 3163 cm^{-1} in the IR spectrum of the ligand. The disappearance of the OH band following coordination can be attributed to the participation of phenolic OH groups in the coordination of HBHTP with M(II) ions.[22,30] The 5–10 cm^{-1} frequency shift of the $\nu_{(\text{aryl–O})}$ stretching peak, found at 1287 cm^{-1} in the free ligand, in the complex spectra provides more evidence for the participation of the deprotonated phenolic OH group in complex formation.[31] Notably, the lattice and coordinated water molecules in the complexes may be responsible for the appearance of a new broadband in the complex spectra, which appeared between 2950 and 2675 cm^{-1}. Upon complexation, the $\nu_{(\text{C=N–N})}$ and $\nu_{(\text{N–N})}$ stretching bands of the hydrazineyl group in the free ligand shifted to higher or lower frequencies than their free-state values of 1634 and 1525 cm^{-1}, respectively, indicating that the HBHTP ligand was coordinated to the M(II) ions *via* the N atom.[22] The IR spectrum of the ligand showed a medium band at 1601 cm^{-1} corresponding to its ν(C=N) thiazole ring; this band was shifted to a lower frequency by approximately 13–25 cm^{-1} following complexation, indicating that it was modified upon coordination with metal ions. The band of the free ligand at 753 cm, assigned to $\nu_{(\text{C–S–C})}$, remained almost unchanged upon complexation, indicating that the sulfur atom was not involved in the coordination with the metal ions.[32] Notably, the IR spectra of the complexes showed FTIR bands in the range – 441–491 cm^{-1}, which corresponded to the stretching vibrations of $\nu_{(\text{M–N})}$. Other bands were observed between 669 and 696 cm^{-1} and were attributed to the stretching vibrations of $\nu_{(\text{M–O})}$.[31] Overall, the IR spectral analysis indicated that the thiazole hybrid ligand (HBHTP, **3**) functioned as a monoanionic (NNO) tridentate ligand.

3.2.3. Ultraviolet-visible spectroscopy (UV-vis) and stability under physiological conditions. The HBHTP ligand and its complexes were analyzed by capturing their electronic absorption spectra in DMSO between 250 nm and 650 nm (Fig. 2B). The absorption spectrum of HBHTP revealed an absorption band at 269 nm corresponding to a π → π* transition. Additionally, strong peaks were observed at 361, 378, and 398 nm, corresponding to n → π* transitions associated with the C=N chromophores of the thiazole ring and azomethine linkage, respectively.[33] Bathochromic shifts were observed in these bands upon complexation, which is evidence of coordination between the thiazole ring and the azomethine group. The electronic spectrum of the CoBHTP complex exhibited a strong peak at 427 nm and a weak band at 599 nm, which can be attributed to the $^4T_{1g}(F) \rightarrow {}^4A_{2g}(P)$ and $^4T_{1g}(F) \rightarrow {}^4T_{1g}(P)$ transitions, respectively. It was hypothesized that the octahedral geometry of the CoBHTP complex is based on its electronic transition pattern, and the experimentally measured magnetic moment of 4.8 BM. The spectral bands at 612 and 417 nm in the NiBHTP complex are attributed to the $^3A_{2g} \rightarrow {}^3T_{2g}$ (F) and $^3A_{2g} \rightarrow {}^3T_{1g}(F)$ transitions, respectively. Furthermore, the hexa-coordinated form of the Ni complex is supported by a magnetic moment value of 2.9 BM, which correlates with the observed transitions.[33] In the UV-vis spectrum of the CuBHTP complex, a significant band was detected at 455 nm, corresponding to the spin-allowed metal-to-ligand charge transfer (MLCT) d → π * transition, in addition to the characteristic ligand peaks. The observed blue shift aligns with previously reported studies.[34,35] This transition is commonly observed in octahedral copper complexes and is accompanied by tailing towards higher wavelengths. Our hypothesis is supported by the fact that the experimentally measured magnetic moment of 1.5 BM was recorded, which also suggests the presence of a molecular interaction that may be created by a coordinating ligand.[36,37]

UV-vis spectral monitoring (for 72 h) under physiological conditions was used to validate the physiological stability of the novel complexes. As depicted in Fig. S5 (ESI†), the UV-vis spectra of the CuBHTP complex did not exhibit any

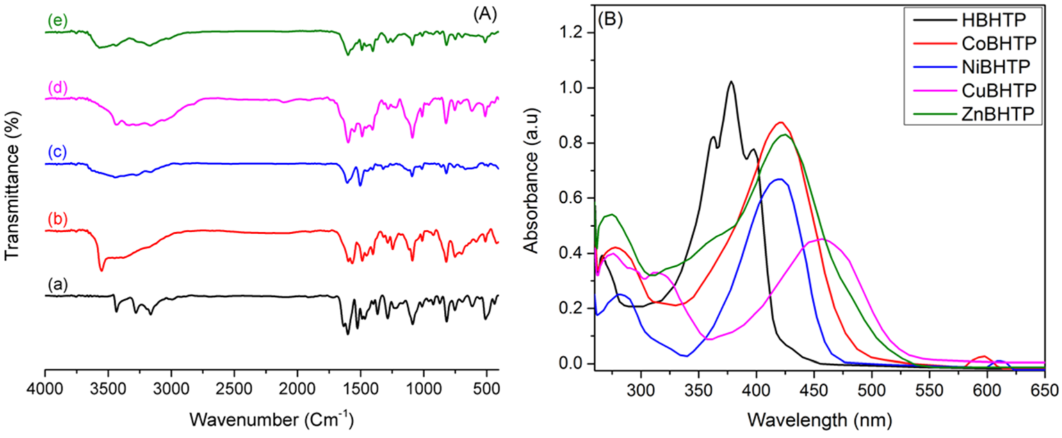

Fig. 2 (A) FTIR spectra of (a) HBHTP, (b) CoBHTP, (c) NiBHTP, (d) CuBHTP, and (e) ZnBHTP; (B) UV-vis spectra of the HBHTP ligand and its complexes in DMSO solution.

significant changes over the storage duration. This observation indicated the remarkable stability of this complex under physiological conditions. The absence of significant alterations in the absorption spectrum throughout the testing period demonstrated that the CuBHTP complex maintained its structural integrity and remained unaffected by time.

3.2.4. NMR spectroscopy. The NMR spectrum of the HBHTP ligand (Fig. S6 and S7, ESI†) provides valuable insights into the structural properties and electronic environment of the compound. Several distinct peaks were observed in the proton NMR spectrum of HBHTP. The two singlets observed at chemical shifts (*δ*) of 11.51 and 78.07 ppm were assigned to the NH and H–C═N moieties of the hydrazine fragments. Additionally, the singlet peak observed at *δ* 7.05 ppm could be attributed to the resonance of the phenolic proton. Finally, the set of signals observed in the chemical shift range of 8.26–6.86 ppm was assigned to the protons of the thiazolyl ring and the chlorobenzylidene moiety.

3.3. *In silico* studies

3.3.1. Geometry optimization, natural bond orbital analysis, and molecular electrostatic potential. The optimized geometrical structures of the parent ligand (HBHTP) and its copper complex (CuBHTP) are shown in Fig. 3A and B, respectively (Table S2, ESI†). Table S3 (ESI†) lists the important bond lengths and angles for both the compounds. The results showed that the CuBHTP complex was formed by coordinating the cupric ion with two monoanionic tridentate (NNO) ligand (HBHTP) molecules in the crystal lattice. Table S3† shows that the complex was distorted octahedrally due to the geometrical bond angles around the copper center: O23–Cu45–N43 (90.01°), O23–Cu45–N21 (90.15°), O1–Cu45–N38 (87.20°), N38–Cu45–N43 (78.89°), O1–Cu45–O23 (100.21°), and N16–Cu45–N38 (71.63°).[38] The bond lengths surrounding cupric ions Cu45–O1 and Cu45–O23 were 1.895 and 1.923 Å, respectively. Similarly, Cu45–N38 and Cu45–N43, with 2.133 Å and 1.977 Å distances, respectively, improved the stability of complex formation. However, the geometrical distortion was also explained by the 3.575 and 2.376 Å Cu45–N16 and Cu45–N21 bond lengths, respectively.

Table S4 (ESI†) summarizes the outcomes of the natural bond orbital (NBOs) analysis for the free ligand and its complex to gain insight into the interaction strength. The results showed that the most negatively charged atoms in HBHTP were O22 = −0.683, N8 = −0.513, N12 = −0.409, and N13 = −0.214. These charges suggest the presence of electron-rich regions in which complexation occurs. The upper-center atom forms an octahedral sphere with N8, N13, and O22 of the two ligand molecules. Cu interacts with the N8 and N13 atoms *via* the P lone-pair orbitals. O22, which has a higher negative charge, participates in complexation and validates electron donation toward the N–Cu coordinate form. The coordination process did not involve N12, a secondary amine group, which may have contributed to intermolecular hydrogen bonding. The electron-rich sites of the complex were O1 = −0.343, O23 = −0.314, N21 = −0.277, N43 = −0.265, and N17 = −0.228.

Molecular electrostatic potential (MEP) was used to demonstrate the surface reactivity of HBHTP and CuBHTP. Fig. 3C and D show the significant reactive sections of the parent ligand (HBHTP) and its complex (CuBHTP), with yellow, orange, red, green, and blue indicating electronic potential values. Red

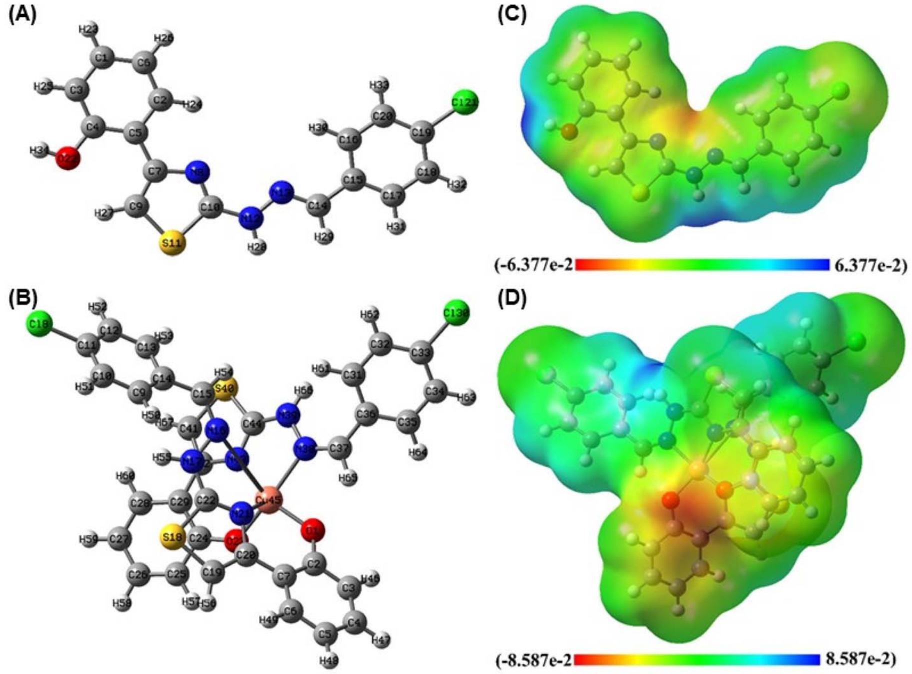

Fig. 3 (A and B) Optimized geometrical structures of (A) the benzylidene–phenol–thiazole (HBHTP) ligand and (B) the copper complex (CuBHTP). (C and D) Molecular electrostatic potentials (MEP) of (C) HBHTP and (D) CuBHTP).

denotes electron-rich (most negative) sites, whereas blue represents electron-poor (most positive) sites.[38] The red curve in HBHTP comprises electron donors N8, N12, and N13, as confirmed by NBO analysis. Nucleophilic attack by N8, N13, and the orange-colored hydroxylic oxygen atom initiated a complex reaction. The oxygen atoms in the electron-rich CuBHTP complex were analyzed using NBOs analysis.

Table 1 Reactivity parameters of HBHTP and CuBHTP in the gas phase with B3LYP/6-311 g(d,p)[a39]

Parameter	HBHTP	CuBHTP
Total energy (a.u)	−1715.035	−3625.335
Dipole moment (debye)	3.194	8.631
E_{HOMO} (eV)	−5.547	−4.769
E_{LUMO} (eV)	−1.882	−2.582
ΔE (eV)	3.665	2.187
I (eV)	5.547	4.769
A (eV)	1.882	2.582
η (eV)	1.832	1.094
μ (eV)	−3.689	−3.675
S (eV)	0.273	0.457
χ (eV)	3.714	3.675
ω (eV)	3.714	6.176

[a] $\Delta E = E_{\mathrm{LUMO}} - E_{\mathrm{HOMO}}$; ionization potential $(I) = -E_{\mathrm{HOMO}}$; electron affinity $(A) = -E_{\mathrm{LUMO}}$; chemical hardness $(\eta) = (I - A)/2$, chemical potential $(\mu) = -(I + A)/2$, electronegativity $(\chi) = -(E_{\mathrm{HOMO}} + E_{\mathrm{LUMO}})/2$, electrophilicity index $(\omega) = \mu^2/2\eta$, global softness $(S) = 1/2\eta$.

3.3.2. Quantum chemical parameters (FMOs analysis, Table 1). The energy gaps of HBHTP and CuBHTP in the gaseous state were estimated by calculating the energies of the highest occupied molecular orbital (HOMO) and lowest unoccupied orbital (LUMO). These results can help to determine the stability of a compound by revealing its molecular reactivity and physicochemical characteristics. Table 1 lists the parameters calculated based on FMO energy values. The ability of a compound to donate electrons to the empty orbital of a receptor molecule is indicated by its high E_{HOMO} value, whereas its low E_{LUMO} value reflects its low electron acceptance resistance.

HBHTP exhibited a high ΔE value of 3.665 eV, suggesting excellent stability and the formation of a less reactive complex. In contrast, CuBHTP displayed a lower ΔE value of 2.187 eV, indicating a higher reactivity and lower stability. The values of I and A are related to E_{HOMO} and E_{LUMO}, respectively, indicating the ability of the compounds to donate or accept electrons. A comparison of CuBHTP and HBHTP revealed that CuBHTP exhibited a lower value (4.769 eV) and higher A value (2.582 eV) than HBHTP. This suggests that the CuBHTP has the potential

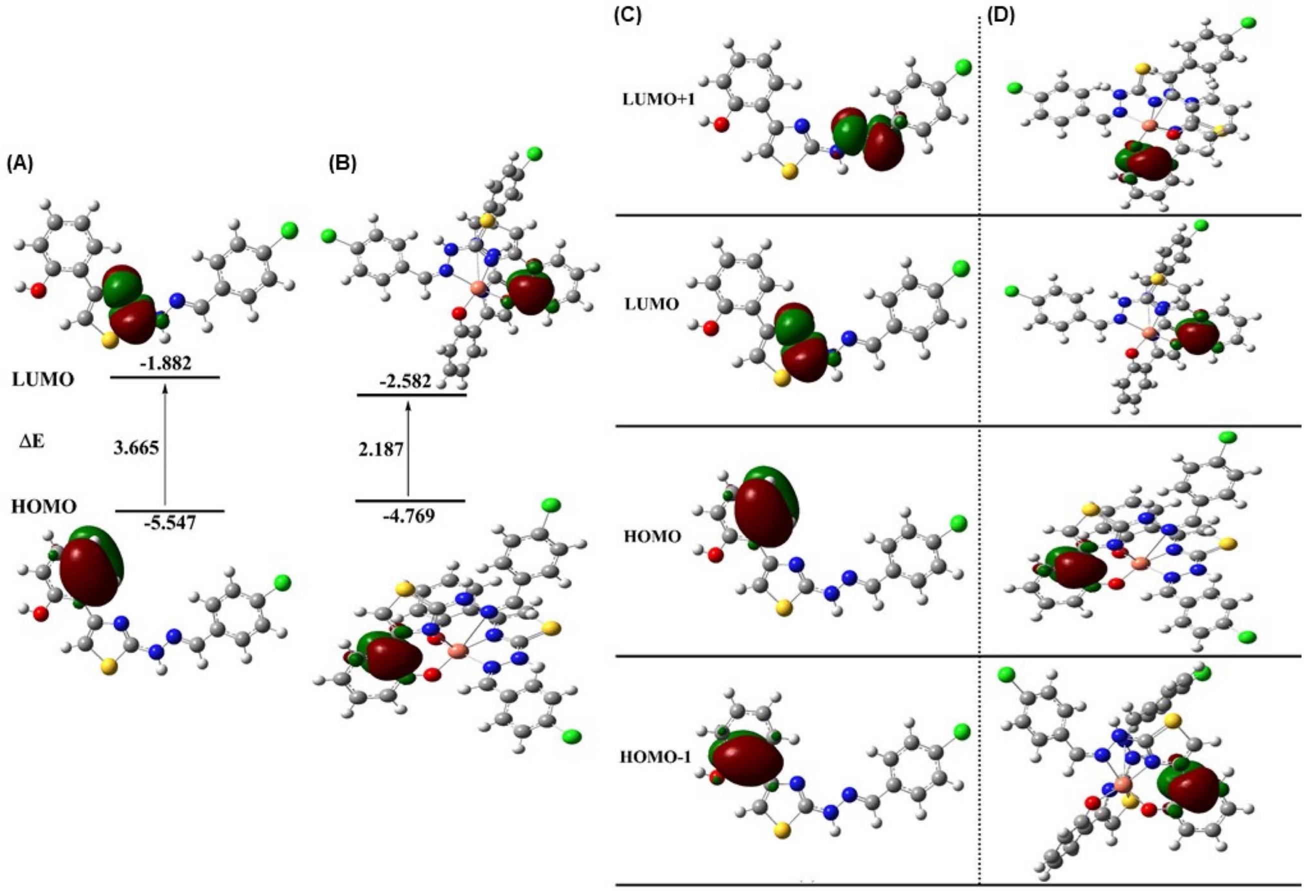

Fig. 4 (A and B) Description of the molecular orbitals with the calculated electronic transitions for (A) HBHTP and (B) CuBHTP. (C and D) Electronic distribution of FMOs for the optimized compounds (C) HBHTP (**3**), (D) CuBHTP (**4c**).

to function as an electron donor. The global reactivity descriptors, namely, chemical hardness and global softness, depend on the parameters I and A, respectively. The compound CuBHTP exhibited a higher S value of 0.457 eV and a lower η value of 1.094 eV than HBHTP, indicating a higher reactivity.[38] The electrophilicity index (ω) quantifies the change in energy of

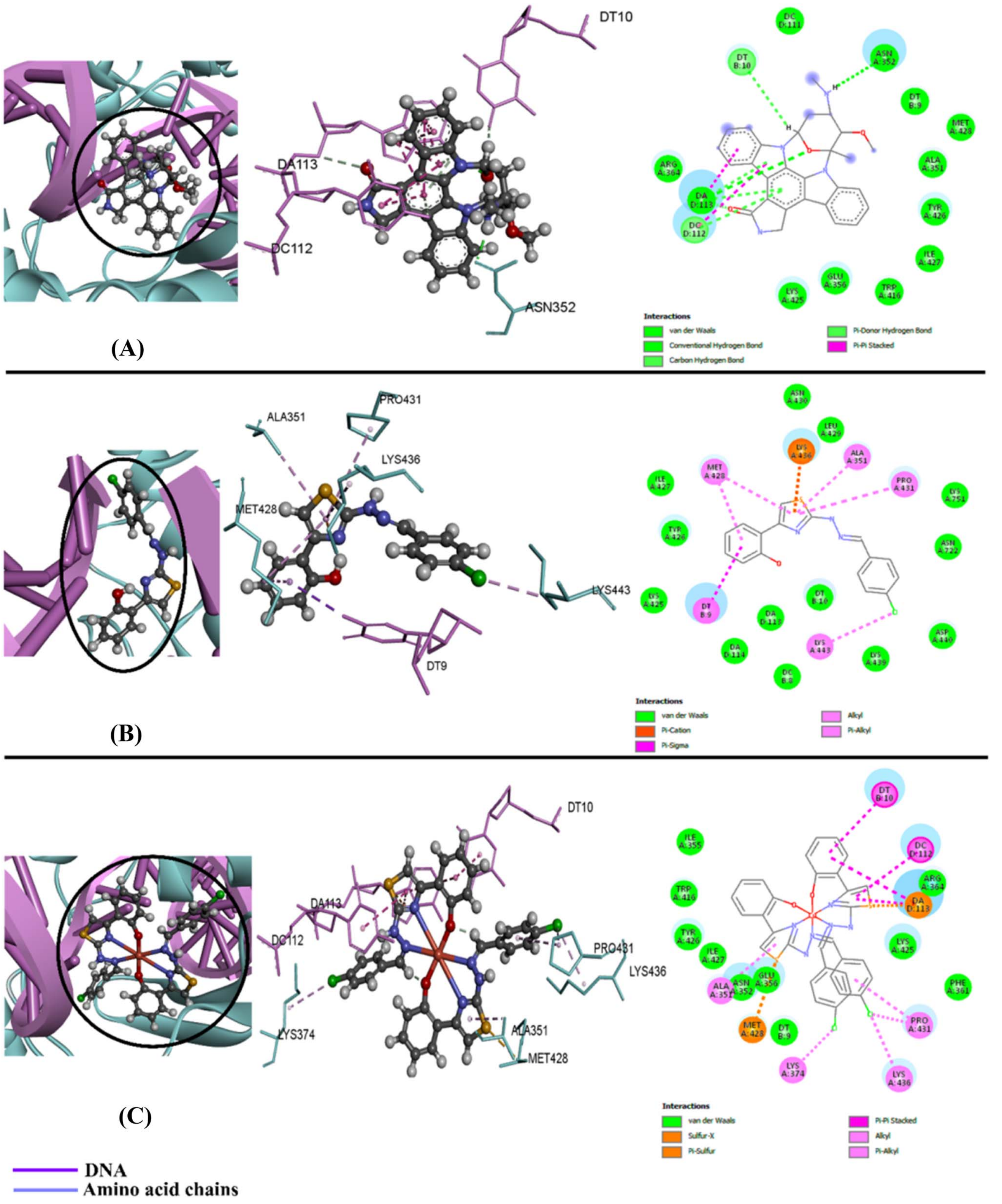

Fig. 5 3D and 2D images of non-covalent interactions (NCIs) resulting from molecular docking of (A) staurosporine, (B) HBHTP, and (C) CuBHTP against the 1T8I receptor.

a system saturated with electrons. Fig. 4A and B show the energy values of the designed compounds. Fig. 4C and D show the HOMO and LUMO electronic orbital densities of the HBHTP and CuBHTP, respectively.

3.3.3. Molecular docking study against topoisomerase I. Topoisomerase I (TOPI) is a vital hybrid enzyme that is involved in DNA strand separation. TOPI comprises four major domains: the subsequent molecular docking process occurs within the residues Glu198 to Ile65, which form the highly conserved "core domain" (54 kDa).[40] HBHTP and CuBHTP were compared with staurosporine, a potent protein kinase C inhibitor that amplifies cAMP-mediated responses in human neuroblastoma cells. The three drug-like compounds were subjected to the same active-site molecular docking simulations. The *in silico* calculations confirmed the results of the MTT cytotoxicity assay, showing that CuBHTP was the best drug-like compound, which scored the lowest binding energy and inhibition constant K_i (-9.64 kcal mol^{-1}, 85.82 nM) compared to its parent, HBHTP (-6.61 kcal mol^{-1}, 14.24 μM), and the reference drug, staurosporine (STP) (-6.63 kcal mol^{-1}, 13.78 μM), as outlined in Table S5 (ESI†). The docking results for all compounds showed a variety of non-covalent interactions (NCIs) generated by protein–ligand complexation, such as van der Waals forces, hydrogen bonding, and electrostatic attractions. H-bonding only appeared in the case of STS in three forms: conventional, carbon, and π-donor H-bonding, as listed in Table S5 (ESI†). Conversely, electrostatic attractions were observed in CuBHTP, ranging from alkyl, π–alkyl, π–sulfur, and π–π stacked attractions to sulfur–X attractions. Molecular docking analysis of HBHTP, CuBHTP, and STP against the 1T8I receptor of TOPI revealed intricate non-covalent interactions (NCIs), which were effectively depicted using both 2D and 3D imaging (Fig. 5). All compounds effectively interacted with similar amino acids and nucleotides, including Asn352(A), Ala351(A), Tyr426(A), and Arg364(A), whereas DA113(D), DC112(D), and DT10(B) exhibited different binding affinities. 3D spatial visualization demonstrated the precise geometric orientation and positioning of the molecules within the active site of TOPI. This visualization illustrates how the structure of CuBHTP may enhance or modify the interaction strength compared with that of a free ligand. The NCIs in the CuBHTP, such as hydrogen bonding, π–π stacking, van der Waals forces, and hydrophobic interactions, exhibited a discernible pattern influenced by the presence of copper ions. Metallic coordination frequently enhances the stabilization effects that are absent in unbound ligands. The 2D representations provide a detailed view of atom-to-atom contacts, showing specific residues within the TOPI active site that directly interact with different parts of the molecular framework of both compounds. In contrast, Fig. S8 (ESI†) shows the hydrophobic interactions of these anticancer agents with different amino acids of the 1T8I receptor, where all compounds exhibited variable levels of hydrophobic interactions.

The free HBHTP ligand predominantly interacts through van der Waals forces with hydrophobic amino acids, such as Ala351, Leu429, and Tyr426, which significantly contributes to the binding affinity by enhancing the molecular fit within the receptor pocket. Conversely, in addition to hydrophobic contacts with Ala35and Ile427, CuBHTP exhibited more robust hydrophobic interactions because of its coordination with the metal center, which induced additional π–π stacking with aromatic residues, such as Tyr426 and Trp416, thus increasing its overall stability when bound to TOPI. Interestingly, CuBHTP demonstrated an optimized design for optimal receptor occupancy and efficacy compared to the reference medication, which only showed hydrophobic interactions with Ala351 and Tyr426.

3.4. Cytotoxicity

The results revealed that the free ligand and its metal complexes exhibited varying degrees of cytotoxicities. Although the free ligand demonstrated moderate cytotoxicity, the metal complexes showed elevated levels of cytotoxicity, with the copper complex (CuBHTP, **4c**) being the most cytotoxic against MCF-7 using IC_{50} (Fig. 6A–C). These findings suggest that the presence of metal ions (particularly Cu(II) ions) in the ligand structure enhances the cytotoxicity. The measured IC_{50} values, which represent the concentration of a compound required to inhibit cell growth by 50%, provided quantitative evidence of the cytotoxic effects of the ligands and their metal complexes. Therefore, CuBHTP exhibited the most significant cytotoxic effects on MCF7 cells compared to other metal ligands (Fig. 7A).

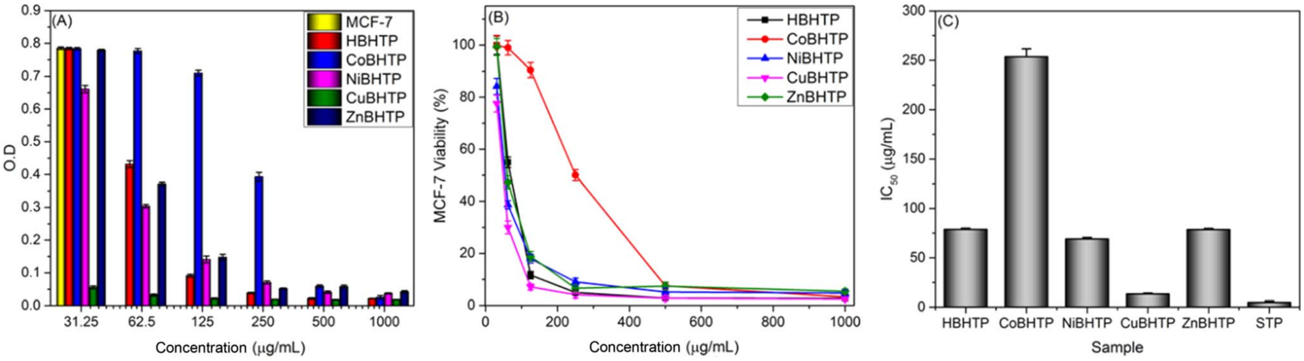

Fig. 6 (A and B) Dose-cytotoxicity correlation in terms of (A) optical density (O.D) and (B) MCF-7 viability; (C) the IC_{50} values (μg mL^{-1}) of the new compounds against MCF-7 cell lines, as compared to a clinical drug (STP).

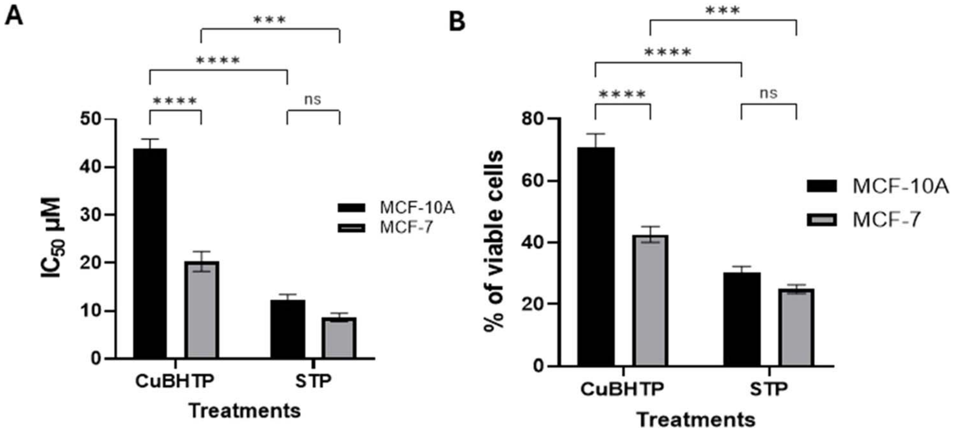

Fig. 7 The impacts of the CuBHTP and staurosporine treatment on MCF7 and MCF10a cell lines. (A) The IC_{50}, (B) the % of viable cells, mean ± SE. *$P < 0.05$, **$P < 0.01$, and ***$P < 0.001$.

Interestingly, by comparing the IC_{50} values of the copper complex (CuBHTP) with those of its analogs (Table S6, ESI†), it was evident that the new complex exhibited a much stronger inhibitory effect on MCF-7 cell growth than the other complexes did. Therefore, a new Cu complex with enhanced cancer cell interactions may improve the anticancer activity in cancer research.

The efficacy of two treatments, CUBHTP and staurosporine (STP), were evaluated on MCF-10A (a normal epithelial breast cell line) and MCF-7 breast cancer cell lines, with potency measured as IC_{50} in μM, where lower values denote higher potency. CUBHTP exhibited an IC_{50} of approximately 40 μM in MCF-10A cells, indicating moderate activity, whereas its IC_{50} in MCF-7 cells was significantly lower, at approximately 10 μM, suggesting a higher potency with a statistically significant difference ($P < 0.001$). Conversely, STP demonstrated greater potency than CUBHTP in both cell lines, with an IC_{50} of approximately 10 μM in MCF-10A cells and an even lower IC_{50} of approximately 5 μM in MCF-7 cells, with a significant difference ($P < 0.001$) (Fig. 7A). Furthermore, the activity of STP in MCF-10A and MCF-7 cells showed no significant difference in activity between the two cell lines, lacking selectivity and revealing toxicity in both normal and cancer cell lines. Both treatments exhibited higher efficacy against MCF-7 cells, with statistically significant results compared with MCF-10A cells, underscoring their potential selectivity for MCF-7 cells. However, CUBHTP exhibited significant selectivity towards cancer cells compared to normal cells.

Additionally, treatment of MCF-10A cells with CUBHTP resulted in cell viability of approximately 70%, suggesting that this treatment effectively maintained a high proportion of viable cells, indicating lower toxicity or a protective effect of the treatment. In contrast, MCF-7 cells treated with CUBHTP exhibited a significantly reduced viability of approximately 40%, with a statistically significant difference ($P < 0.001$) compared to MCF-10A cells, highlighting CUBHTP's selective toxicity of CUBHTP toward MCF-7 cells while sparing MCF-10A cells. Conversely, STP treatment resulted in lower overall cell viability, with MCF-10A cells exhibiting approximately 40% and MCF-7 cells at approximately 30% viability, indicating that STP is more toxic to both cell lines. The difference in viability between MCF-10A and MCF-7 cells upon STP treatment was not significant ("ns"), indicating that STP did not exhibit selective toxicity in the two cell lines (Fig. 7B). Therefore, CUBHTP demonstrated a greater ability to protect MCF-10A cells (70% viability) than MCF-7 cells (40% viability), with a significant difference, whereas STP showed less protective capacity, with viabilities of 40% and 30% for MCF-10A and MCF-7 cells, respectively, with no significant selectivity. Thus, CUBHTP was more effective at maintaining MCF-10A cell viability when targeting MCF-7 cells. These findings are consistent with those of previous studies, indicating that the synthesized compound may serve as a targeted chemotherapeutic agent for tumor cells with chromosomal aberrations, developmental traits, and cancer-related expression characteristics.[41] CuBHTP showed potential as a therapeutic agent against breast cancer MCF-7 cells while sparing non-tumorigenic MCF-10A cells, consistent with studies showing that compounds can selectively induce cytotoxicity in cancer cells through metabolic differences.[42] STP exhibited non-selective toxicity, affecting both MCF-10A and MCF-7 cells, without significant differences in viability. This lack of selectivity may limit STP's therapeutic use of STP as it can damage healthy cells during chemotherapy.[43] The differential response to CUBHTP may be attributed to the overexpression of receptors in MCF-7 cells targeted by the compound.[44] Further studies are needed to elucidate CUBHTP's molecular targets of CUBHTP for clinical application.

Copper(II) complexes have emerged as promising anticancer agents owing to their redox activity, which generates reactive oxygen species (ROS) that target cancer cells.[45] A copper(II) hydrazone complex showed an IC_{50} of 7.14 ± 0.05 μM against MCF-7 cells.[46] Another copper(II) Schiff base complex had an IC_{50} of 10 μM with an SI of 2.[19] The CuBHTP complex (IC_{50} 5.2 μM, SI 4.2) shows enhanced potency through DNA binding and topoisomerase I inhibition by thiazole and phenol moieties. Cobalt(II), nickel(II), and zinc(II) complexes showed varied efficacies, with a cobalt(II) hydrazone complex showing an IC_{50} of 15 μM against MCF-7 cells.[47] A nickel(II) salphen complex showed an IC_{50} of approximately 20 μM against MCF-7 cells, but demonstrated high selectivity for quadruplex DNA (>50-fold).[48] Zinc(II) hydrazone complexes have IC_{50} values ranging from approximately 8 to 10 μM in MCF-7 cells, although they often lack selectivity.[49]

Cisplatin, a conventional platinum-based chemotherapeutic agent, shows an IC_{50} of 5.9–20 μM against MCF-7 cells. However, its clinical use is limited by its toxicity to normal cells (SI ∼1–2) and resistance development.[19] CuBHTP exhibited a comparable or lower IC_{50} and higher SI values than cisplatin, indicating its advantage over cisplatin in terms of toxicity. Its multi-targeted mechanisms, including DNA adduct formation, topoisomerase I inhibition, and modulation of aromatase, SULF1,2, and bFGF gene expression, offer a broader scope than the DNA cross-linking mechanism of cisplatin. Compared to staurosporine, CuBHTP showed higher selectivity (SI: 4.2 *vs.* 2.5) and inhibited Hsp90 and tubulin β. CuBHTP demonstrated high potency ($IC_{50} = 5.2$ μM), selectivity (SI = 4.2), and multi-targeted activity, addressing toxicity and resistance. UV-vis spectroscopy confirmed the stability of CuBHTP in the assay medium, ensuring the activity of the intact complex.[45] Notably, certain iridium(III) complexes with N-heterocyclic carbene ligands have achieved sub-micromolar IC_{50} values (0.3–4.8 μM) against K562 cells, surpassing the efficacy of cisplatin.[50] Therefore, CuBHTP presents significant advantages over cisplatin, staurosporine, and other metal complexes because of its potency, selectivity, and multi-targeting mechanisms. These findings highlight the potential of the HBHTP platform in the development of novel anticancer agents.

3.5. Inhibitory effects of CuBHTP on aromatase (CYP19A)

Human aromatase (HA), which is key to estrogen synthesis, is a potential candidate for endocrine therapy of breast cancer. Aromatase inhibitors (AIs) block HA activity and reduce blood estrogen levels. AIs includes steroidal and nonsteroidal blockers, with steroidal blockers as natural HA substrates. Hormone therapy, which suppresses estrogen levels, is crucial in breast cancer treatment.[51]

The results showed that CuBHTP substantially inhibited cytochrome 19A (CYP 19A) in MCF-7 cancer cells ($P < 0.001$), whereas letrozole significantly suppressed aromatase expression ($P < 0.0001$) (Fig. 8A). Although the activity of CuBHTP was lower than that of letrozole, it effectively suppressed aromatase with fewer adverse effects, meeting the clinical therapy needs. Understanding the structure of human aromatase could help in the development of innovative treatment candidates.[52]

3.6. Effect of CuBHTP on the quantitative expression of Hsp90 and P53

Moreover, MCF-7 cells showed high expression of Hsp90, and CuBHTP significantly reduced this expression ($P < 0.001$) compared to novobiocin, which reduced the expression ($P < 0.01$) (Fig. 8B). Condelli *et al.*[53] revealed that the expression of heat shock proteins (HSPs), also known as molecular chaperones, increases in cells exposed to stressors, such as heat shock, chemical agents, and pathological abnormalities. According to Whitesell and Lindquist,[54] the potential application of Hsp90 chaperones in cancer treatment has been emphasized, with the proposal that HSP90 inhibitors could be utilized as standalone therapies or in conjunction with other treatments. Furthermore, Condelli *et al.*[53] found that HSP90α is crucial in cellular processes such as energy consumption, survival, and signalling, and its presence facilitates the invasion and migration of various cancer cells in both laboratory and living organisms.[31,55]

CuBHTP elevated P53 expression in MCF7 cancer cells beyond the effects of cisplatin, leading to G1 phase arrest and reduced G2/M phase, apoptosis, and DNA repair (Fig. 8C). P53 mutations affect DNA binding and stability, thereby reducing the function associated with tumor development. Addressing these changes is crucial for effective tumor management.[56] CuBHTP, a promising chemotherapeutic agent, restricts HSP90 expression in breast cancer cells, elevates thermoregulation,

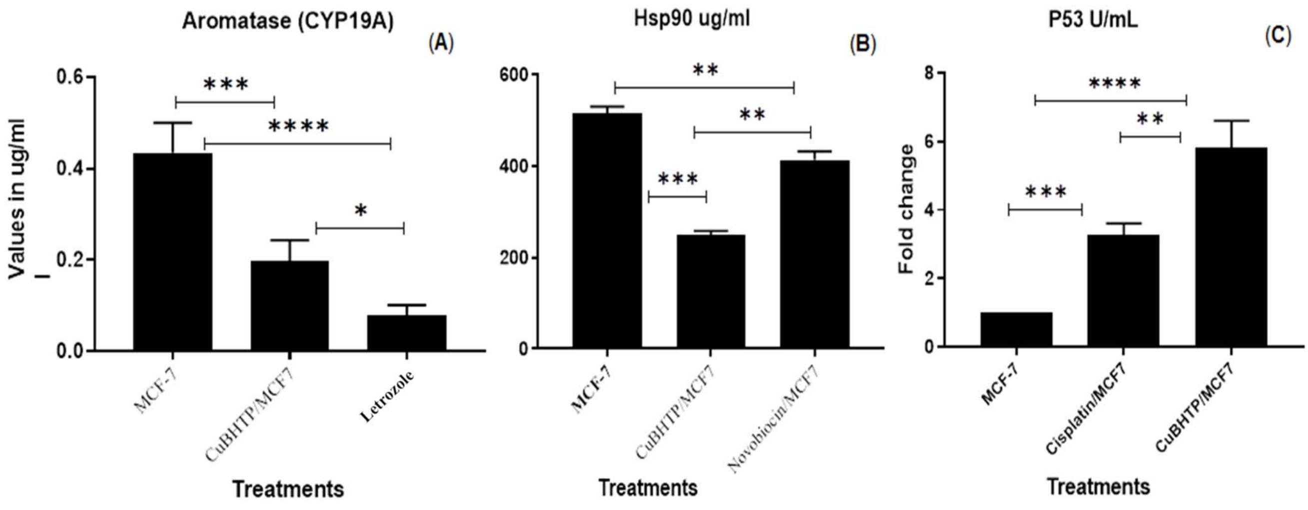

Fig. 8 (A) Inhibitory activity of CuBHTP and letrozole on CYP19A; (B) inhibitory role of CuBHTP on Hsp90 in comparison to novobiocin; (C) upregulating effect on P53 expression in comparison to cisplatin, mean ± SE. *$P < 0.05$, **$P < 0.01$, and ***$P < 0.001$.

and augments P53 for disease eradication. Its role in apoptosis *via* P53 elevation and G1 phase arrest may involve Cu(II) and its active ligands. Alvarez *et al.*[57] identified ligands with bi- and tri-thiazole groups in Cu complexes, showing C–H···Cl interactions that enabled the deformed copper cores to form binuclear copper complexes during crystallization. Reduced Hsp90 and increased p53 levels are associated with decreased RNA synthesis in cancer cells.[58] Studies have shown that major chaperones, such as Hsp proteins, stabilize p53 by reducing its exposure to proteolytic enzymes in the proteasome.[59]

These chaperones are important targets for the anticancer activity of chemotherapeutic drugs and for cancer treatment. However, Hsps have been implicated in cancer progression and resistance to anticancer therapies.[60] Under stress, Hsp synthesis increases, facilitating protein folding and suppressing hydrophobic structures associated with significant protein damage.[61]

3.7. Effect of CuBHTP on tubulin β enzyme activity expression

Analysis of the effects of MCF-7, CUBHTP, and colchicine on tubulin β levels (μg mL^{-1}) (Fig. 9) showed that MCF-7 cells exhibited the highest expression of tubulin β at approximately 5 μg mL^{-1}, whereas CUBHTP and colchicine showed lower levels (2 μg mL^{-1}). Statistical analysis revealed significant differences between MCF-7 cells treated with both CUBHTP and colchicine ($P < 0.001$), whereas CUBHTP and colchicine showed no significant difference in their impact on tubulin β levels. The elevated expression of tubulin β in MCF-7 cells can be effectively suppressed by CUBHTP, as well as by colchicine.

This suggested that its activity may be attributed to its interaction with the tubulin/microtubule system and its ability to impede cell division. The antimitotic mechanism may involve binding to α/β-tubulin heterodimers or polymer.[62] Colchicine binds to β-tubulin at the colchicine-binding site of the α–β-tubulin dimer interface, inhibits tubulin polymerization, and prevents microtubule assembly, thereby leading to mitotic arrest. Stanton *et al.*[63] showed colchicine binds to β-tubulin with high affinity ($K_d \approx 1$ μM), disrupting microtubule dynamics by stabilizing the tubulin dimer. This mechanism was confirmed by Ravelli *et al.*,[64] who reported that CuBHTP inhibited tubulin β better than colchicine, which has toxicity limitations. Colchicine disrupts cellular processes in normal and cancerous cells by binding to β-tubulin, causing side effects, such as gastrointestinal toxicity, bone marrow suppression, and neurotoxicity. Finkelstein *et al.*[65] The narrow therapeutic index of colchicine causes dose-limiting toxicity, with gastrointestinal effects in 80% of patients. Extended exposure can cause multiorgan failure, as noted by Nuki,[66] in patients with renal or hepatic impairment.

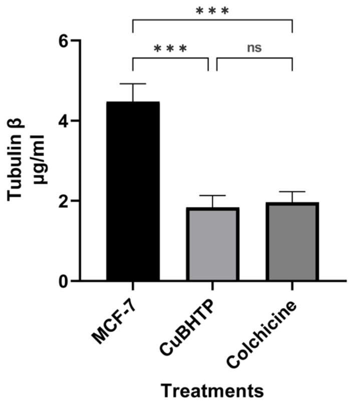

Fig. 9 Role of CuBHTP on tubulin β enzyme levels in MCF7 cells, mean ± SE. *$P < 0.05$, **$P < 0.01$, and ***$P < 0.001$.

Microtubules play a critical role in cellular processes such as cell shape, transportation, and chromosome segregation during mitosis and meiosis, forming mitotic spindles that are crucial for proper cellular function.[67] Leandro-García *et al.*[68] reported a high incidence of TUBB3 overexpression in brain cancer, other solid tumor types,[69] and ovarian cancer.[70,71] Consequently, chemotherapeutic agents that inhibit tumor cell microtubule synthesis and impede their function by blocking mitotic spindle fibers culminate in programmed cell death in both solid tumors and hematological cancers.[46] Narvi *et al.*[72] suggested that increased microtubule dynamics associated with TUBB3 could potentially result in resistance to drugs that target the microtubules.

3.8. Effect of CuBHTP on cell content and cell cycle phases

The effectiveness of the synthesized compounds in inhibiting MCF-7 cell growth depends on their ability to decrease DNA content and assess cell cycle progression through cell cycle arrest and cell growth inhibition in MCF-7 cells.[73] MCF-7 cells were exposed to CuBHTP at a concentration equivalent to its IC$_{50}$ value for 24 h. As shown in Fig. 10, CuBHTP treatment significantly reduced the number of MCF-7 cells, leading to a decrease in the proportion of cells in the G0/G1 phase from 61.43% to 55.12%, and an increase in the proportion of cells in the G2/M phase from 24.76% to 33.41%. Additionally, the proportion of cells in the S phase decreased from 13.803% to 11.47% compared with that of the untreated cells.

The DNA content across different cell cycle phases (MCF7, CuBHTP/MCF7, NQO1, and STP/M) was used to assess the activity of CuBHTP and STP. In MCF7 cells, the DNA content distribution was 61.43% in G0/G1, 24.76% in S, and 13.81% in G2/M, indicating a high proportion of cells in G0–G1 phase, suggesting active cell division. For CuBHTP/MCF7 treated, the distribution shifted to 55.12% in G0/G1, 33.41% in S, and 11.47% in G2/M, showing a slight increase in G0/G1 and decrease in G2/M, which may indicate that CuBHTP induces partial arrest in G0/G1, slowing progression to G2/M (Fig. 10II(A)). Önem *et al.*[74] revealed that purpurin combined with Cu(II) can cause DNA damage by generating ROS and forming DNA adducts through the Cu(I)/Cu(II) redox cycle, which may involve both mechanisms of carcinogenic effects. The effects of different treatments on MCF-7 cells were evaluated by measuring necrosis and early and late apoptosis using Annexin V-FITC staining. In the cancer control group, the distribution was 4.76% necrosis, 8.22% early apoptosis, and 15.97% late apoptosis, indicating minimal necrosis. In the CuBHTP/MCF7 treatment, necrosis decreased to 1.96%, early apoptosis 0.27%, and late apoptosis remained low at 0.14%,

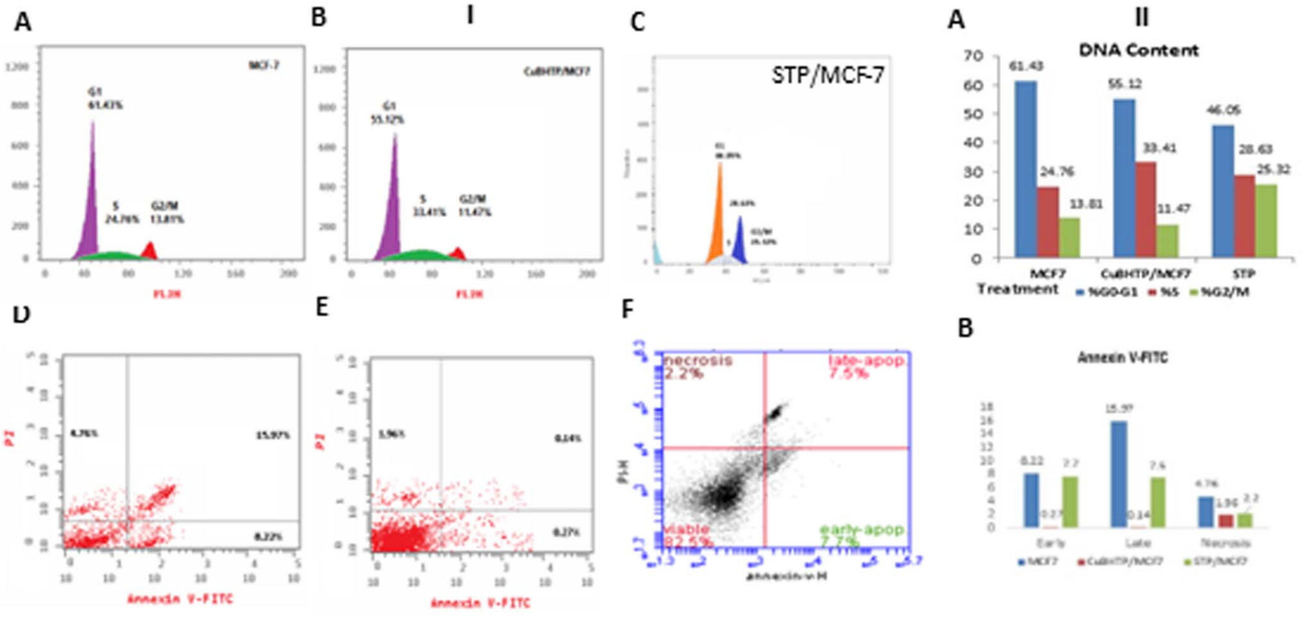

Fig. 10 Effect of CuBHTP on the cell cycle and apoptosis as determined by flow cytometry analysis. (I (A–F)) Cell cycle and (II (A)) DNA content and (B) Annexin V-FITC for apoptosis.

suggesting that CuBHTP induced a moderate increase in early apoptosis, with a slight increase in necrosis. For the STP/MCF7 treatment, necrosis was 2.2%, early apoptosis was 7.7%, and late apoptosis was 7.5%, showing a slight increase in necrosis and early apoptosis compared to the control, but with no significant late apoptosis (Fig. 10IIB). Overall, CuBHTP appeared to be effective in promoting early apoptosis and necrosis in MCF-7 cells, whereas both treatments had a limited effect on late apoptosis.

3.9. Quantitative real-time (qRT-PCR) estimation of gene expression

The effects of CuBHTP and staurosporine (STP) on MCF-7 cells were investigated for the expression of SULF1, SULF2, bFGF, TOPI, and TOPII. The treatment with CuBHTP resulted in a 1.2-fold increase. SULF1 and SULF2 showed fold changes of 0.7 and 0.5, with SULF2 reduction being significant ($P < 0.001$) and SULF1 less significant ($P < 0.05$). bFGF expression was decreased by 0.3-fold ($P < 0.001$). TOPI and TOPII showed 0.6-fold changes, with TOPI showing a significant reduction ($P < 0.001$), and TOPII showing moderate significance ($P < 0.01$) (Fig. 11A). CuBHTP significantly downregulated SULF2, bFGF, and TOPI expression, and had moderate effects on TOPII and SULF1 in MCF-7 cells. The downregulation of SULF2 and bFGF ($P < 0.001$) suggests interference with sulfatase activity and growth factor signalling and inhibiting proliferation and metastasis.[75] The reduction in TOPI expression ($P < 0.001$) and TOPII ($P < 0.01$) implies that CuBHTP may inhibit DNA replication and transcription, akin to the action of topoisomerase inhibitors, such as camptothecin.[76] These findings suggest the potential of CuBHTP as a multi-target cancer therapeutic agent. CuBHTP inhibited topoisomerase I (TOPI) and II (TOPII) in MCF-7 cells, as indicated by the reduced gene expression. This aligns with research where 4-benzoylthiosemicarbazides demonstrated TOPI and TOPII inhibition, with IC_{50} values of approximately 50 μM in MCF-7 cells.[77] The mechanism of action of CuBHTP likely involves stabilization of the TOP–DNA complex, preventing DNA re-ligation, and inducing apoptosis. Treatment with STP of MCF-7 cells reduced SULF1 and SULF2 expression, with fold changes of 0.7 ($P < 0.01$) and 0.6 ($P < 0.001$), respectively. bFGF expression decreased by 0.4 ($P < 0.001$), whereas TOPI and TOPII showed fold changes of 0.6, with TOPI showing a significant reduction ($P < 0.001$) and TOPII showing moderate significance ($P < 0.01$) compared to MCF-7 cells (Fig. 11B). STP significantly downregulated SULF2, bFGF, and TOPI; moderately affected SULF1 and TOPII; and slightly upregulated MCF-7 cells. Staurosporine, a protein kinase inhibitor, exhibits broad-spectrum inhibitory effects. Downregulation of SULF2 and bFGF may disrupt sulfatase activity and growth factor signalling, potentially inhibiting cancer cell growth.[78] The reduction in TOPI and TOPII expression is consistent with previous studies, indicating that staurosporine interferes with DNA replication and transcription.[79] These results underscore STP's potential of STP as an anticancer agent and indicate that its non-selective nature could affect normal cells. Comparative analysis of the effects of CuBHTP and staurosporine (STP) on MCF-7 gene expression revealed their distinct activities. For SULF1, CuBHTP reduced its expression to approximately 0.7, whereas STP decreased it to approximately 0.6. Both compounds downregulated SULF2, with CuBHTP reducing it to ∼0.5, and STP reducing it to ∼0.6. bFGF was suppressed by both agents, with CuBHTP exhibiting a greater effect (∼0.3) than STP (∼0.4). For TOPI and TOPII, both compounds reduced the expression to ∼0.6. CuBHTP demonstrated strong or comparable inhibitory effects on SULF2, TOPIFGF, TOPI, and TOPII, whereas STP was more effective in suppressing SULF1. These findings suggested that

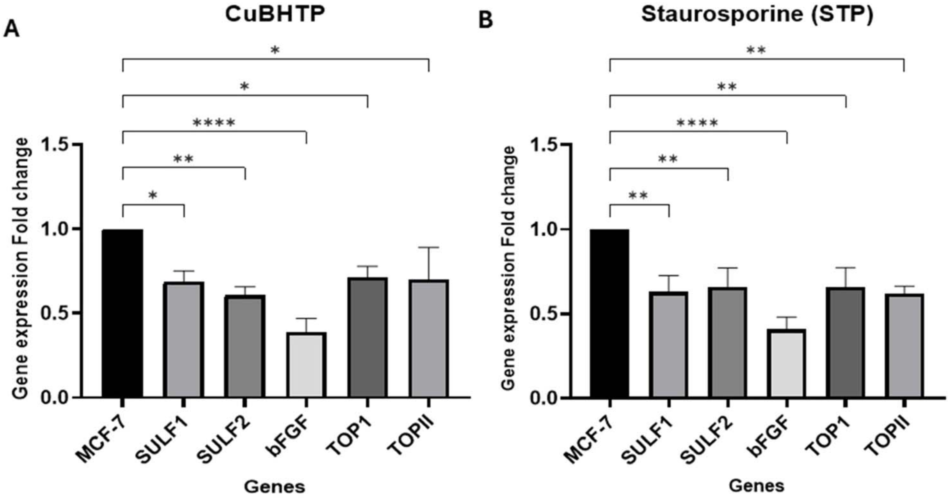

Fig. 11 (A and B) Effect of CuBHTP and staurosporine treatment on SULF1, 2, and bFGF, TopI, II gene expression in MCF7 breast cancer cells, mean ± SE. *$P < 0.05$, **$P < 0.01$, and ***$P < 0.001$.

CuBHTP may have a more targeted inhibitory profile than broader-acting STP.

Xu *et al.*[80] stated that Sulf-1 plays a crucial role in regulating cell growth and death, making it a target for hepatocellular carcinoma therapy. Cancer cells initiate survival pathways. Inhibition of SULF1 and 2 suppresses growth factor signalling, contributing to chemotherapeutic activity.[81,82] High SULF1 and SULF2 expression levels are correlated with poor prognosis with SULF1 priority dysregulated in HNSCC tissues and SULF2 promotes tumor growth by increasing fibroblast growth factor 7, which activates the PI3K/AKT and MAPK/ERK pathways to induce cell cycle progression.[83,84]

Topoisomerase I inhibits cell proliferation and causes cell cycle arrest in the G1 and G2 phases of the cell cycle. Oxocrebanine catalytically inhibits DNA degradation. The levels of TOPI and II are modulated by CuBHTP, and targeting these enzymes has anticancer potential. According to Wang and Tse-Dinh,[2] TOP I and II inhibitors have limitations, including resistance and adverse effects. The authors have proposed dual inhibitors that target both enzymes. An additional aromatic ring enhances DNA intercalator affinity and increases cytotoxicity. Qian *et al.*[85] found aminothiazonaphthalimide forms a DNA complex with anti-tumor activity in lung cancer cells. Bharti *et al.*[86] reported copper(II) complexes cleave DNA *via* increased hydroxyl radical production, implying that DNA is largely free from RNA and proteins.

Benzylidene–phenol–thiazole (HBHTP) metal complexes, specifically CuBHTP, target multiple pathways in breast cancer *via* topoisomerase I (TOPI) inhibition. Topoisomerase II (TOPII) aids breast cancer progression *via* DNA replication,[4] while TOPI resolves DNA supercoiling during transcription.[87] TOPI inhibitors, such as camptothecin derivatives, are effective against metastatic breast cancer by stabilizing the TOPI–DNA cleavage complex and inducing DNA breaks and apoptosis.[88] Molecular docking studies have shown that CuBHTP binds strongly to TOPI through thiazole and phenol moieties,[77] complementing its DNA adduct (CT DNA adducts covalent modifications of DNA that occur when carcinogens or reactive chemicals bind to cytosine (C) and thymine (T) bases in DNA. These adducts can disrupt normal DNA replication and transcription, potentially leading to mutations, cancer or other genetic damage) formation, p53 upregulation, and Hsp90 and tubulin β inhibition. Targeting TOPI offers advantages over TOPII inhibitors, such as anthracyclines, which face resistance due to TOPII downregulation.[89] CuBHTP significantly inhibited TOPI, coupled with G1 and S phase arrest and the upregulation of apoptotic markers, supporting its efficacy. Future research should explore the activity of CuBHTP against TOPII for its dual-targeting potential.[4]

The MCF-7 cell line (ER+/PR+/HER2−) was selected to evaluate the anticancer activity of M(II)–HBHTP complexes because of its widespread use in screening metal-based anticancer agents, enabling comparison with literature IC$_{50}$ values.[19] CuBHTP exhibited potent cytotoxicity against MCF-7 cells (IC$_{50}$ = 5.2 ± 0.3 μM) with high selectivity (SI = 4.2 *vs.* MCF10A), indicating sensitivity to its mechanisms, including topoisomerase I (TOPI) inhibition. Gene expression analyses and molecular docking confirmed TOPI inhibition and downstream effects (p53 upregulation), validating the utility of MCF-7 cells despite their moderate TOPI expression.[88] However, MCF-7 cells express lower levels of TOPI and TOPII than aggressive cell lines, such as MDA-MB-231, which may limit their relevance for TOP inhibitor studies.[89] Therefore, targeting TOPI with CuBHTP is justified by its role in breast cancer, the docking-confirmed binding affinity of CuBHTP, and its potential to overcome TOPII inhibitor resistance in breast cancer cells. The MCF-7 cell line, despite moderate TOPI expression, was appropriate for the initial screening, highlighting the potential of CuBHTP as a TOPI-targeted anticancer agent and warranting further mechanistic and preclinical studies.

4 Conclusion

Chemotherapeutic research has shifted towards non-platinum-based compounds as anticancer medications with reduced toxicity. Copper compounds are of interest because of their endogenous nature and their DNA-damaging potential in humans. A novel ligand, the benzylidene–phenol–thiazole hybrid (HBHTP), was synthesized using a hybrid pharmacophore strategy. M(II) complexes were created and validated using FT-IR, UV-vis, and NMR spectroscopies. CuBHTP was the most active compound, exhibiting the lowest toxicity in MCF-10A cells. The copper complex exhibited superior cytotoxicity against MCF-7 breast cancer cells ($IC_{50} = 5.2$ μM) with high selectivity ($SI = 4.2$) compared to MCF10A cells, outperforming that of staurosporine ($SI = 2.5$). CuBHTP inhibited aromatase and reduced Hsp90 expression more effectively than novobiocin while upregulating P53 beyond the effects of cisplatin. It suppressed tubulin β, SULF1, SULF2, and bFGF gene expression, with significant reductions in SULF2, bFGF, and topoisomerase I (TOPI) expression ($P < 0.001$). CuBHTP induced cell cycle arrest in the G1 and S phases, reduced the DNA content, and promoted apoptosis (early: 8.22%; late: 15.97%). Molecular docking revealed that CuBHTP strongly binds to TOPI (-9.64 kcal mol^{-1}), stabilizing TOPI–DNA complexes. Structural characterization validated the stability of the complexes, while *in silico* analyses supported CuBHTP reactivity. Compared to cisplatin and staurosporine, CuBHTP exhibited enhanced potency, selectivity, and multi-targeted activity. This study demonstrates the potential of CuBHTP as TOPIOP1-targeted chemotherapeutic agent, although it is limited by its *in vitro* scope and evaluation in MCF-7 and MCF10A cells. However, further *in vivo* studies are required to confirm this hypothesis.

5 Study limitations

Although a study on benzylidene–phenol–thiazole (HBHTP) and its Cu(II) complex (CuBHTP) showed promising anticancer activity against MCF-7 cells, several limitations were observed. This study focused on *in vitro* cytotoxicity and molecular docking and did not include *in vivo* validation in animal models. Assessment of topoisomerase I expression is limited to molecular docking and gene expression data, without enzymatic activity assays. This study evaluated only the MCF-7 and MCF10A cell lines, limiting insights across cancer types. The mechanisms underlying the regulation of P53, Hsp90, tubulin β, SULF1,2, and bFGF have not yet been fully elucidated. Moreover, long-term effects on cell cycle arrest and resistance mechanisms have not been investigated. Future studies should address these gaps through *in vivo* experiments, using a broader range of cell lines, and mechanistic analysis. Future modifications to HBHTP, such as the incorporation of electron-donating groups, may further reduce the IC_{50} of CuBHTP, as suggested by the structure–activity relationship studies.

Data availability

The data supporting the findings of this study are available upon request from the corresponding author. The data were not publicly available due to privacy or ethical restrictions.

Conflicts of interest

The authors declare no conflicts of interest.

Acknowledgements

The authors extend their appreciation to Umm Al-Qura University, Saudi Arabia for funding this research work through grant number: 25UQU4331270GSSR01.

References

1 F. Bray, J. Ferlay, I. Soerjomataram, R. L. Siegel, L. A. Torre and A. Jemal, *Ca-Cancer J. Clin.*, 2018, **68**, 394–424.
2 W. Wang and Y.-C. Tse-Dinh, *Curr. Top. Med. Chem.*, 2019, **19**, 730–740.
3 M. Will, J. Liang, C. Metcalfe and S. Chandarlapaty, *Nat. Rev. Cancer*, 2023, **23**, 673–685.
4 Y. Pommier, *ACS Chem. Biol.*, 2013, **8**, 82–95.
5 J. J. Champoux, *Annu. Rev. Biochem.*, 2001, **70**, 369–413.
6 Y. Seol, H. Zhang, Y. Pommier and K. C. Neuman, *Proc. Natl. Acad. Sci. U. S. A.*, 2012, **109**, 16125–16130.
7 B. Zhao, P. Liu, T. Fukumoto, T. Nacarelli, N. Fatkhutdinov, S. Wu, J. Lin, K. M. Aird, H.-Y. Tang, Q. Liu, D. W. Speicher and R. Zhang, *Nat. Commun.*, 2020, **11**, 908.
8 I. Mancini, J. Vigna, D. Sighel and A. Defant, *Molecules*, 2022, **27**, 4948.
9 H. Kantarjian, E. Jabbour, J. Grimley and P. Kirkpatrick, *Nat. Rev. Drug Discov.*, 2006, **5**, 717–718.
10 P.-C. Lv, K.-R. Wang, Y. Yang, W.-J. Mao, J. Chen, J. Xiong and H.-L. Zhu, *Bioorg. Med. Chem. Lett.*, 2009, **19**, 6750–6754.
11 M. Anjalin, N. Kanagathara and A. R. B. Suganthi, *Mater. Today: Proc.*, 2020, **33**, 4751–4755.
12 S. K. Bharti, S. K. Patel, G. Nath, R. Tilak and S. K. Singh, *Transition Met. Chem.*, 2010, **35**, 917–925.
13 A. Rauf, M. K. Kashif, B. A. Saeed, N. A. Al-Masoudi and S. Hameed, *J. Mol. Struct.*, 2019, **1198**, 126866.
14 K. A. Scott, P. B. Cox and J. T. Njardarson, *J. Med. Chem.*, 2022, **65**, 7044–7072.
15 G. C. Tron, T. Pirali, G. Sorba, F. Pagliai, S. Busacca and A. A. Genazzani, *J. Med. Chem.*, 2006, **49**, 3033–3044.
16 V. Thamilarasan, N. Sengottuvelan, A. Sudha, P. Srinivasan and G. Chakkaravarthi, *J. Photochem. Photobiol., B*, 2016, **162**, 558–569.
17 M. J. Hannon, *Chem. Soc. Rev.*, 2007, **36**, 280–295.
18 K. S. Kasprzak, F. W. Sunderman Jr and K. Salnikow, *Mutat. Res., Fundam. Mol. Mech. Mutagen.*, 2003, **533**, 67–97.
19 C. Marzano, M. Pellei, F. Tisato and C. Santini, *Anti-Cancer Agents Med. Chem.*, 2009, **9**, 185–211.
20 C. Hoppe, S. Kutschan, J. Dörfler, J. Büntzel, J. Büntzel and J. Huebner, *Clin. Exp. Med.*, 2021, **21**, 297–313.
21 F. A. Cotton, G. Wilkinson, C. A. Murillo and M. Bochmann, *Advanced Inorganic Chemistry*, John Wiley & Sons, 1999.
22 S. Saydam and E. Yilmaz, *Spectrochim. Acta, Part A*, 2006, **63**, 506–510.

23 G. M. Morris, R. Huey, W. Lindstrom, M. F. Sanner, R. K. Belew, D. S. Goodsell and A. J. Olson, *J. Comput. Chem.*, 2009, **30**, 2785–2791.

24 M. Y. Alfaifi, M. A.-E. Zein, A. A. Shati, M. A. Alshehri, S. E. I. Elbehairi, H. S. Hafez and R. F. M. Elshaarawy, *J. Photochem. Photobiol., A*, 2019, **385**, 112083.

25 E. İnce Ergüç, S. Özcan Sezer and H. Gürer Orhan, *Turk. J. Pharm. Sci.*, 2022, **19**, 626–629.

26 T. Zhu, S.-H. Wang, D. Li, S.-Y. Wang, X. Liu, J. Song, Y.-T. Wang and S.-Y. Zhang, *Bioorg. Med. Chem. Lett.*, 2021, **37**, 127698.

27 T. Xiaoling, M. A. Ashraf and Z. Yanyan, *Pak. J. Pharm. Sci.*, 2016, **29**, 2169–2172.

28 M. Roederer, Z. Darzynkiewicz and D. R. Parks, *Methods Cell Biol.*, 2004, **75**, 241–256.

29 S. A. Bustin, *AZ of Quantitative PCR*, International University Line, La Jolla, CA, 2004, vol. 5.

30 M. Y. Alfaifi, S. E. I. Elbehairi, H. S. Hafez and R. F. M. Elshaarawy, *J. Mol. Struct.*, 2019, **1191**, 118–128.

31 S. E. I. Elbehairi, M. Y. Alfaifi, A. A. Shati, M. A. Alshehri, R. F. M. Elshaarawy and H. S. Hafez, *Chem. Biol. Drug Des.*, 2020, **96**, 1148–1161.

32 R. F. M. Elshaarawy, T. B. Mostafa, A. A. Refaee and E. A. El-Sawi, *RSC Adv.*, 2015, **5**, 68260–68269.

33 S. Abubakar, G. A. Shallangwa and I. Abdulkadir, *J. Umm. Al-qura Univ. Appl. Sci.*, 2024, **10**, 613–623.

34 A. A. Alzharani, *J. Umm. Al-qura Univ. Appl. Sci.*, 2023, **9**, 455–470.

35 E. Chiyindiko, E. H. G. Langner and J. Conradie, *Molecules*, 2022, **27**, DOI: 10.3390/molecules27186033.

36 A. A. Awaji, H. W. Alhamdi, K. M. Alshehri, M. Y. Alfaifi, A. A. Shati, S. E. I. Elbehairi, N. A.-F. Radwan, H. S. Hafez, R. F. M. Elshaarawy and M. Welson, *J. Inorg. Biochem.*, 2025, **262**, 112720.

37 R. F. M. Elshaarawy and C. Janiak, *Arabian J. Chem.*, 2016, **9**, 825–834.

38 H. A. Elbadawy, A. E. Ali, A. A. Elkashef, S. Foro and D. S. El-Sayed, *Appl. Organomet. Chem.*, 2022, **36**, e6793.

39 G. T. Tigineh, M. Abiye, A. Melese and A. Abebe, *Chem. Biol. Drug Des.*, 2023, **101**, 479–488.

40 A. Lauria, M. Ippolito and A. M. Almerico, *J. Mol. Model.*, 2007, **13**, 393–400.

41 X. Zheng, X. Gai, S. Han, C. D. Moser, C. Hu, A. M. Shire, R. A. Floyd and L. R. Roberts, *Genes, Chromosomes Cancer*, 2013, **52**, 225–236.

42 U. Anand, A. Dey, A. K. S. Chandel, R. Sanyal, A. Mishra, D. K. Pandey, V. De Falco, A. Upadhyay, R. Kandimalla, A. Chaudhary, J. K. Dhanjal, S. Dewanjee, J. Vallamkondu and J. M. Pérez de la Lastra, *Genes Dis.*, 2023, **10**, 1367–1401.

43 A. Burguin, C. Diorio and F. Durocher, *J. Pers. Med.*, 2021, **11**, 808.

44 B. Kinnel, S. K. Singh, G. Oprea-Ilies and R. Singh, *Cancers*, 2023, **15**, 1320.

45 C. Santini, M. Pellei, V. Gandin, M. Porchia, F. Tisato and C. Marzano, *Chem. Rev.*, 2014, **114**, 815–862.

46 P. T. Lim, B. H. Goh and W.-L. Lee, 3 - Taxol: Mechanisms of action against cancer, an update with current research, *Paclitaxel*, ed. M. K. Swamy, T. Pullaiah and Z.-S. Chen, Academic Press, 2022, pp. 47–71, ISBN 9780323909518, DOI: 10.1016/B978-0-323-90951-8.00007-2.

47 P. Kumari, B. Ghosh and S. Biswas, *J. Drug Targeting*, 2016, **24**, 179–191.

48 R. Paprocka, M. Wiese-Szadkowska, S. Janciauskiene, T. Kosmalski, M. Kulik and A. Helmin-Basa, *Coord. Chem. Rev.*, 2022, **452**, 214307.

49 S.-R. Li, Y.-M. Tan, L. Zhang and C.-H. Zhou, *Pharmaceutics*, 2023, **15**, 1348.

50 P. Štarha, *Inorg. Chem. Front.*, 2025, **12**, 897–954.

51 G. Zucchini, E. Geuna, A. Milani, C. Aversa, R. Martinello and F. Montemurro, *Int. J. Women's Health*, 2015, **7**, 551–563.

52 W. L. Miller, *Trends Endocrinol. Metab.*, 2017, **28**, 771–793.

53 V. Condelli, F. Crispo, M. Pietrafesa, G. Lettini, D. S. Matassa, F. Esposito, M. Landriscina and F. Maddalena, *Cells*, 2019, **8**, 532.

54 L. Whitesell and S. L. Lindquist, *Nat. Rev. Cancer*, 2005, **5**, 761–772.

55 R. Bershawy, H. S. Hafez, S. S. El-Sakka, A. Hammad and M. H. Soliman, *J. Biomol. Struct. Dyn.*, 2023, **42**(23), 12885–12899.

56 X. Wang, X. Song, W. Zhuo, Y. Fu, H. Shi, Y. Liang, M. Tong, G. Chang and Y. Luo, *Proc. Natl. Acad. Sci. U. S. A.*, 2009, **106**, 21288–21293.

57 N. Alvarez, F. Velluti, F. Guidali, G. Serra, M. G. Kramer, J. Ellena, G. Facchin, L. Scarone and M. H. Torre, *Inorg. Chim. Acta*, 2020, **508**, 119622.

58 S. Zhang, C. Wang, B. Ma, M. Xu, S. Xu, J. Liu, Y. Tian, Y. Fu and Y. Luo, *Cell Rep.*, 2020, **32**(1), 107879.

59 L. Dubrez, S. Causse, N. Borges Bonan, B. Dumétier and C. Garrido, *Oncogene*, 2020, **39**, 516–529.

60 S. Yang, H. Xiao and L. Cao, *Biomed. Pharmacother.*, 2021, **142**, 112074.

61 B. J. Lang, M. E. Guerrero, T. L. Prince, Y. Okusha, C. Bonorino and S. K. Calderwood, *Arch. Toxicol.*, 2021, **95**, 1943–1970.

62 B. C. Parker, M. Engels, M. Annala and W. Zhang, *J. Pathol.*, 2014, **232**, 4–15.

63 E. T. Rosolowsky, J. Skupien, A. M. Smiles, M. Niewczas, B. Roshan, R. Stanton, J. H. Eckfeldt, J. H. Warram and A. S. Krolewski, *J. Am. Soc. Nephrol.*, 2011, **22**, 545–553.

64 R. B. G. Ravelli, B. Gigant, P. A. Curmi, I. Jourdain, S. Lachkar, A. Sobel and M. Knossow, *Nature*, 2004, **428**, 198–202.

65 Y. Finkelstein, S. E. Aks, J. R. Hutson, D. N. Juurlink, P. Nguyen, G. Dubnov-Raz, U. Pollak, G. Koren and Y. Bentur, *Clin. Toxicol.*, 2010, **48**, 407–414.

66 G. Nuki, *Curr. Rheumatol. Rep.*, 2008, **10**, 218–227.

67 E. R. Smith, J.-Q. Wang, D.-H. Yang and X.-X. Xu, *Drug Resistance Updates*, 2022, **65**, 100881.

68 L. J. Leandro-García, S. Leskelä, I. Landa, C. Montero-Conde, E. López-Jiménez, R. Letón, A. Cascón, M. Robledo and C. Rodríguez-Antona, *Cytoskeleton*, 2010, **67**, 214–223.

69 M. C. Tsourlakis, P. Weigand, K. Grupp, M. Kluth, S. Steurer, T. Schlomm, M. Graefen, H. Huland, G. Salomon, T. Steuber,

W. Wilczak, H. Sirma, R. Simon, G. Sauter, S. Minner and A. Quaas, *Am. J. Pathol.*, 2014, **184**, 609–617.

70 G. Ferrandina, G. F. Zannoni, E. Martinelli, A. Paglia, V. Gallotta, S. Mozzetti, G. Scambia and C. Ferlini, *Clin. Cancer Res.*, 2006, **12**, 2774–2779.

71 Y. Koh, B. Jang, S.-W. Han, T.-M. Kim, D.-Y. Oh, S.-H. Lee, C. H. Kang, D.-W. Kim, S.-A. Im, D. H. Chung, Y. T. Kim, T.-Y. Kim, Y.-W. Kim, J. H. Kim, D. S. Heo and Y.-J. Bang, *J. Thorac. Oncol.*, 2010, **5**, 320–325.

72 E. Narvi, K. Jaakkola, S. Winsel, C. Oetken-Lindholm, P. Halonen, L. Kallio and M. J. Kallio, *Br. J. Cancer*, 2013, **108**, 82–90.

73 D. Kaminskyy, A. Kryshchyshyn and R. Lesyk, *Eur. J. Med. Chem.*, 2017, **140**, 542–594.

74 A. N. Önem, K. Sözgen Başkan and R. Apak, *ACS Omega*, 2023, **8**, 5103–5115.

75 C. Zhu, L. He, X. Zhou, X. Nie and Y. Gu, *Oncol. Rep.*, 2016, **35**, 1318–1328.

76 S. Mastrangelo, G. Attina, S. Triarico, A. Romano, P. Maurizi and A. Ruggiero, *Biomed. Pharmacol. J.*, 2022, **15**, 553–562.

77 J. L. Delgado, C.-M. Hsieh, N.-L. Chan and H. Hiasa, *Biochem. J.*, 2018, **475**, 373–398.

78 M. Tenhagen, P. J. Van Diest, I. A. Ivanova, E. Van Der Wall and P. Van Der Groep, *Endocr.-Relat. Cancer*, 2012, **19**, 115–129.

79 M. W. Karaman, S. Herrgard, D. K. Treiber, P. Gallant, C. E. Atteridge, B. T. Campbell, K. W. Chan, P. Ciceri, M. I. Davis and P. T. Edeen, *Nat. Biotechnol.*, 2008, **26**, 127–132.

80 G. Xu, W. Ji, Y. Su, Y. Xu, Y. Yan, S. Shen, X. Li, B. Sun, H. Qian, L. Chen, X. Fu, M. Wu and C. Su, *Oncotarget*, 2014, **5**, 5029–5039.

81 W. Ji, J. Yang, D. Wang, L. Cao, W. Tan, H. Qian, B. Sun, Q. Qian, Z. Yin, M. Wu and C. Su, *PLoS One*, 2011, **6**, e23274.

82 H. Liu, X. Fu, W. Ji, K. Liu, L. Bao, Y. Yan, M. Wu, J. Yang and C. Su, *Hepatol. Res.*, 2013, **43**, 516–525.

83 D.-Y. Liu, X.-M. Shen, F.-F. Yuan, O.-Y. Guo, Y. Zhong, J.-G. Chen, L.-Q. Zhu and J. Wu, *Mol. Neurobiol.*, 2015, **52**, 1467–1476.

84 T. Jian, Z. H. Chen, Z. Chen and D. Tan, *Braz. J. Med. Biol. Res.*, 2020, **53**(2), 8901.

85 X. Qian, Z. Li and Q. Yang, *Bioorg. Med. Chem.*, 2007, **15**, 6846–6851.

86 S. K. Bharti and S. K. Singh, *Med. Chem. Res.*, 2014, **23**, 1004–1015.

87 J. C. Wang, *Nat. Rev. Mol. Cell Biol.*, 2002, **3**, 430–440.

88 Y. Pommier, E. Leo, H. Zhang and C. Marchand, *Chem. Biol.*, 2010, **17**, 421–433.

89 J. L. Nitiss, *Nat. Rev. Cancer*, 2009, **9**, 338–350.